Formation and Thermal Stability of Platinum Oxides on Size-Selected Platinum Nanoparticles: Support Effects

L. K. Ono,[†] B. Yuan,[‡] H. Heinrich,[†,‡] and B. Roldan Cuenya*[,†]

Department of Physics, Advanced Materials Processing and Analysis Center, University of Central Florida, Orlando, Florida 32816, United States

Received: September 11, 2010; Revised Manuscript Received: October 31, 2010

This article presents a systematic study of the formation and thermal stability of Pt oxide species on size-selected Pt nanoparticles (NPs) supported on SiO_2, ZrO_2, and TiO_2 thin films. The studies were carried out in ultrahigh vacuum (UHV) by temperature-dependent X-ray photoelectron spectroscopy (XPS) measurements and ex situ transmission electron microscopy and atomic force microscopy. The NPs were synthesized by inverse micelle encapsulation and oxidized in UHV at room temperature by an oxygen plasma treatment. For a given particle size distribution, the role played by the NP support on the stability of Pt oxides was analyzed. PtO_2 species are formed on all supports investigated after O_2-plasma exposure. A two-step thermal decomposition ($PtO_2 \rightarrow PtO \rightarrow Pt$) is observed from 300 to 600 K upon annealing in UHV. The stability of oxidized Pt species was found to be enhanced on ZrO_2 under annealing treatments in O_2. Strong NP/support interactions and the formation of Pt−Ti−O alloys are detected for Pt/TiO_2 upon annealing in UHV above 550 K but not under an identical treatment in O_2. Furthermore, thermal treatments in both environments above 700 K lead to the encapsulation of Pt by TiO_x. The final shape of the micellar Pt NPs is influenced by the type of underlying support as well as by the post-deposition treatment. Spherical Pt NPs are stable on SiO_2, ZrO_2, and TiO_2 after in situ ligand removal with atomic oxygen at RT. However, annealing in UHV at 1000 K leads to NP flattening on ZrO_2 and to the diffusion of Pt NPs into TiO_2. The stronger the nature of the NP/support interaction, the more dramatic is the change in the NP shape ($TiO_2 > ZrO_2 > SiO_2$).

Introduction

Supported platinum nanoparticles (NPs) are of scientific and technologic relevance due to their applications in the field of catalysis for a variety of processes including the oxidation of CO and hydrocarbons in automotive catalytic converters, the oxidation of NH_3 in nitric acid synthesis, hydrosilylation of alkenes and aryl alkynes, hydrogenation of benzene and cyclohexene, and direct decomposition and oxidation of alcohols.[1−11]

The microscopic understanding of the mechanisms and chemical kinetics underlying heterogeneous catalytic processes over supported NPs is a challenging task.[12] Among the many factors that influence the reactivity of a NP are its oxidation state[9,13] and support.[7,14] NP-support interactions are known to drastically affect the catalytic performance of metal NPs by modifying their electronic and structural properties,[7,15,16] by influencing the shape of the supported NPs,[17,18] by providing new active sites (e.g., perimeter),[19] or by encapsulation.[20−23] The stoichiometry and relative stability of oxidized Pt compounds that can be formed on the surface of Pt single crystals[24−28] and mono/bimetallic NPs,[7−9,29] as well as their role in the reactivity of Pt is still under debate. Oxidized Pt surfaces have been suggested to be more reactive than metallic Pt for CO oxidation.[13,30−32] For example, Dam et al.[33] have shown that Pt dissolution in fuel cells is reduced when a protective platinum oxide layer is present, and Hull et al.[34] reported high reactivities for PtO_x(shell)/Pt(core)-carbon nanotube catalysts. Nevertheless, other authors attribute the temporal decay in the performance of Pt-based fuel cell electrodes to the formation of PtO and subsequent Pt dissolution.[35] In addition, the formation of PtO_x species of volatile nature have been suggested as responsible for the enhanced coarsening of Pt NPs[36,37] upon annealing in O_2 as compared to H_2.

The main objective of the present in situ study is to provide insight into the interaction of oxygen with supported size-selected Pt NPs, revealing the initial stages of oxidation and the changes in the stoichiometry of the PtO_x species formed under various thermal treatments in UHV and oxygen atmospheres.

The formation and stability of PtO and PtO_2 species on bulk Pt single crystals, Pt thin films and Pt powders has been profusely investigated in the past.[38−43] Additional stoichiometries and different structures, including Pt_2O_3, Pt_3O_4, α-PtO_2, β-PtO_2, and β′-PtO_2 have also been recently reported.[5,44] The following standard enthalpies of formation of the different bulk Pt oxide phases can be found in the literature: PtO (−71 kJ/mol), Pt_3O_4 (−268 ± 100 kJ/mol), and PtO_2 (−134 ± 42 kJ/mol).[45,46] On the basis of such values, the stability of the different bulk oxides can be roughly estimated after normalization by the number of oxygen atoms, leading to the following trend: $Pt_3O_4 > PtO_2 > PtO$.[5,44] However, such trend corresponds to bulk Pt oxide phases, and it might not be representative of oxide phases formed on small Pt NPs.[7,10,47] In addition, even for bulk Pt, PtO_2 is the most commonly reported stable oxide.[48−52] For instance, Held et al.[53] described the formation of Pt_xO_y oxide clusters with a stoichiometry *x*:*y* close to 1:1 after oxygen adsorption on Pt(531), and assigned this to the Pt_3O_4 phase. These clusters were observed to be highly active for CO oxidation.[44,53] Density functional calculations (DFT) by Seriani et al.[5] on bulk Pt oxides

* To whom correspondence should be addressed. E-mail: roldan@physics.ucf.edu.
[†] Department of Physics.
[‡] Advanced Materials Processing and Analysis Center.

10.1021/jp1086703
Published on Web 11/23/2010

revealed the superior stability of Pt_3O_4 as compared to PtO_2 with the following thermal decomposition trend: $PtO_2 \rightarrow Pt_3O_4 \rightarrow Pt$.[54,55] However, previous work from our group reported PtO as the dominant species stabilized on Pt NPs supported on nanocrystalline oxides after annealing treatments in air and O_2.[7,10,47] In addition, the relative content of Pt oxide species on monometallic Pt NPs was found to depend on the NP size,[8] as well as on the degree of reducibility of the oxide support[7,56] and in bimetallic Pt−M NPs (M = Au, Pd, Ru, and Fe) on the oxygen affinity of the secondary metal.[9] By comparing a number of nanocrystalline oxide powder supports (SiO_2, TiO_2, ZrO_2, Al_2O_3, etc.), Croy et al.[7] observed the more facile reduction of PtO_x species, formed upon sample annealing in air, when deposited on TiO_2 substrates. However, open questions remained with respect to the relative thermal stability of the PtO and PtO_2 species formed, and a more in-depth in situ temperature-dependent study was found to be needed. Similar trends were also observed when oxidized Au NPs (Au_2O_3/Au) supported on SiO_2 and TiO_2 were annealed in UHV.[56] For a nearly identical initial particle size distribution, Au_2O_3 compounds formed on these NPs were found to be more stable when the clusters were deposited on SiO_2, as compared to TiO_2.[56] In the latter case, it was suggested that oxygen vacancies present on the TiO_2 surface were replenished upon sample annealing by O atoms spilling-over to the NP/support interface.

The present study provides insight into the chemical nature and thermal stability of oxide species formed over size-selected supported Pt NPs, via XPS, after in situ exposure to atomic oxygen. Emphasis is given to discussing the role played by the NP support. We will address the following questions: (1) Are PtO_2 and PtO compounds formed on small Pt NPs and do they coexist at certain temperatures? (2) Is PtO_2 directly reduced to Pt^0 or does the decomposition involve PtO as intermediate species? (3) Are Pt−O−M compounds formed at the NP/support interface and under which conditions? (4) What type of NP/support interactions are present for each of our material systems (NP encapsulation by the support, NP/support interfacial alloy formation, etc.)? (5) Does the NP support influence the final shape of the supported NPs after distinct post-deposition treatments (e.g., atomic oxygen exposure at RT, annealing in UHV or O_2)?

Experimental Details

Pt NPs were synthesized within micelles of polystyrene-block-poly(2-vinylpyridine) diblock copolymers [PS(*x*)-*b*-P2VP(*y*), Polymer Inc.]. Inverse micelles with the polar units (P2VP) constituting the core and the nonpolar polystyrene (PS) tails extending outward are formed when PS-*b*-P2VP polymers are dissolved in toluene. These micelles are then loaded with a metal salt, chloroplatinic acid ($H_2PtCl_6 \cdot 6H_2O$), which attaches to the pyridine groups in the P2VP core. This sample preparation method results in narrow NP size-distributions with well-defined interparticle distances and a homogeneous coverage of the NPs in practically any substrate.[47] The NP size and interparticle distance can be tuned by changing the molecular weight of the diblock copolymer core (P2VP) and tail (PS), respectively. Further size control of the NPs can be gained by tuning the relative metal salt/P2VP concentration ratio (*r*). In this study, a PS(27700)-P2VP(4300) polymer was used, and $r = 0.6$. A more detailed description of the preparation method can be found elsewhere.[56−58] Naturally oxidized Si(001) wafers and oxidized polycrystalline ultrathin Ti and Zr films electron-beam evaporated on Si(001) have been used as NP supports. According to cross sectional transmission electron microscopy (TEM) images, the thicknesses of the support oxide films investigated are SiO_2(4 nm), ZrO_2(6 nm), and TiO_2(7 nm). These substrates were dip-coated in the Pt-polymeric solution at a speed of 10 mm/min.

The ex situ prepared samples were transferred into a UHV system (SPECS GmbH) for polymer removal and in situ electronic and chemical characterization via monochromatic XPS (Al K_α, 1486.6 eV). Polymer etching from the NPs' surface was conducted by O_2-plasma exposure at RT at a pressure of 4.0×10^{-5} mbar for 100 min in the same UHV system where the subsequent sample characterization was carried out. This treatment also results in the oxidation of the Pt NPs. XPS measurements were conducted immediately after the exposure to atomic oxygen and no detectable amounts of C-1s (285.2 eV), N-1s (399.3 eV), or Cl-2s (270.0 eV) from the P2VP and H_2PtCl_6 salt were observed.[57]

The morphology of the samples before and after polymer removal as well as after the different annealing treatments was characterized ex situ by atomic force microscopy (AFM) in tapping-mode (Digital Instruments, Nanoscope III). Further morphological and structural characterization was carried out by cross sectional TEM and scanning TEM (STEM) with an acceleration voltage of 300 kV (Tecnai F30). TEM cross-sectional samples were prepared using a focused ion beam (FIB) system (FEI 200TEM). The error margins given for the AFM NP heights correspond to the calculated standard deviation. Nevertheless, the NP sizes reported are reproducible when multiple samples are prepared by dip-coating different pieces of the same type of substrate on a given NP solution. A description of the samples investigated is given in Table 1.

The temperature-dependent decomposition of platinum oxides on NPs supported on different substrates was studied in situ by XPS after isochronal annealing in 50 K-steps from RT to 1000

TABLE 1: Description of Pt NP Samples Synthesized Using the Technique of Inverse Micelle Encapsulation and Deposited on Different Oxide Supports[a]

substrate	sample	treatment	particle height (nm) AFM [TEM]	particle diameter (nm) TEM	aspect ratio: height/diameter
SiO_2(4 nm)/Si(001)	# 1a	O_2-plasma	2.6 ± 0.4 [3.0 ± 0.8]	3.1 ± 0.8	1.0 ± 0.1
	# 1b	anneal in UHV, 1000 K	2.7 ± 0.4 [3.1 ± 0.3]	3.1 ± 0.3	1.0 ± 0.1
	# 1c	anneal in O_2, 1000 K	1.5 ± 0.2		
ZrO_2(6 nm)	# 2a	O_2-plasma	1.5 ± 0.4 [2.8 ± 0.3]	2.9 ± 0.2	1.0 ± 0.1
	# 2b	anneal in UHV, 1000 K	2.1 ± 0.6 [2.9 ± 0.7]	3.8 ± 0.7	0.7 ± 0.1
	# 2c	anneal in O_2, 1000 K	1.4 ± 0.4		
TiO_2(7 nm)/Ti(6 nm)	# 3a	O_2-plasma	3.3 ± 0.6 [2.5 ± 0.2]	2.8 ± 0.2	1.0 ± 0.1
	# 3b	anneal in UHV, 1000 K	1.2 ± 0.3		
	# 3c	anneal in O_2, 1000 K			

[a] The average NP heights (AFM, TEM) and diameters (TEM) obtained after an O_2-plasma treatment, annealing in UHV and in O_2 ($P[O_2] = 1 \times 10^{-4}$ mbar) at 1000 K are given.

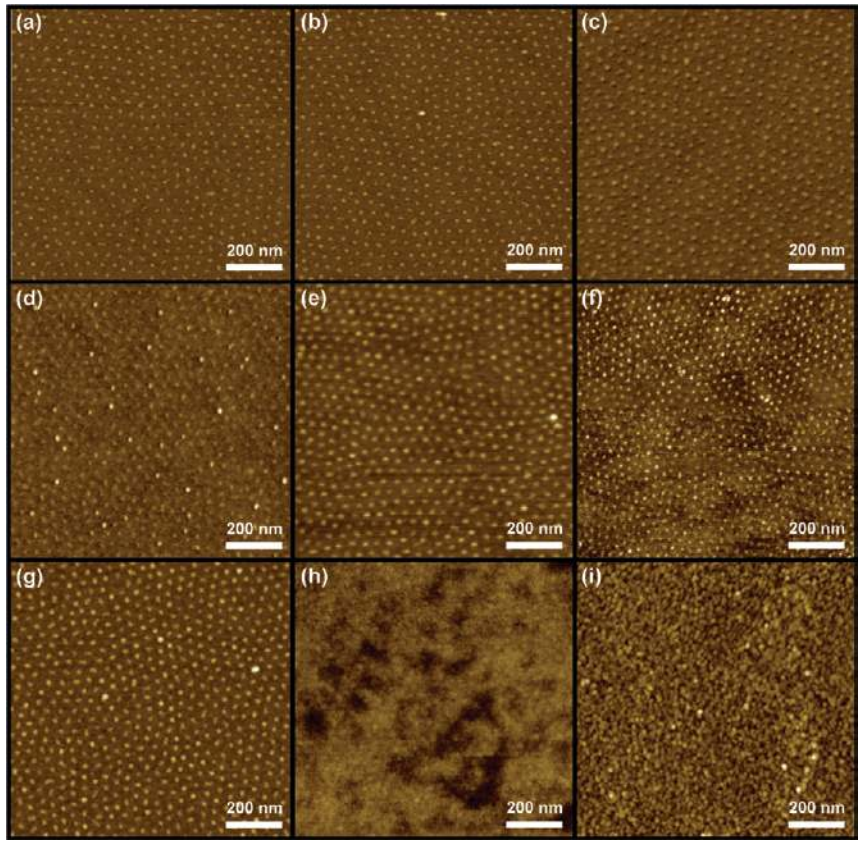

Figure 1. $1 \times 1\ \mu m^2$ tapping mode AFM images of (a−c) Pt/SiO_2(4 nm)/Si(001), (d−f) Pt/ZrO_2(6 nm)/SiO_2/Si(001), and (g−i) Pt/TiO_2(7 nm)/Ti(6 nm) synthesized by inverse micelle encapsulation. The images were acquired after O_2-plasma exposure (a,d,g), and after annealing in UHV at 1000 K (b,e,h) and in O_2 environment (1×10^{-4} mbar) (c,f,i). The height scale in all images is $z = 8$ nm.

K. A linear heating ramp of $\beta = 3$ K/s was used to achieve the desired temperature, and the target temperatures were maintained for 10 min. XPS spectra were acquired at RT after each thermal treatment. The XPS binding energy (BE) scale was calibrated using the Si^0-$2p_{3/2}$ (99.3 eV) [Pt/SiO_2/Si(001), Pt/ZrO_2(6 nm)/SiO_2/Si(001)] and Ti^0-$2p_{3/2}$ (454.0 eV) [Pt/TiO_2/Ti/SiO_2/Si(001)] peaks as reference.[56,59,60] The ultrathin nature of our oxide supports allows us to observe the signal of the underlying reduced substrates [Ti^0 in the TiO_2/Ti films and Si^0 in SiO_2/Si(001) and ZrO_2/SiO_2/Si(001)]. An additional experiment was conducted to monitor whether the sample exposure to the X-ray beam at RT would also induce a partial decomposition of the Pt oxides (PtO_2 and PtO) formed via the O_2-plasma treatment. Only a slight reduction of PtO_2 (∼3%) and no reduction of PtO were observed at RT after X-ray exposure for 120 min under our experimental conditions (Al K_α, 1486.6 eV radiation and a power of 300 W), Supporting Information Figure 1. The 120 min exposure time used in the latter experiments is longer than the acquisition time (∼10 min) required to measure each of the XPS spectra shown in this work. Therefore, any X-ray-induced decomposition of Pt-oxides can be ruled out. For the quantitative analysis of peak positions, line widths, and relative areas of the Pt^0, Pt^{2+}, and Pt^{4+} species, the raw XPS spectra were fitted with six Gaussian−Lorentzian functions (three doublets) using the CASA XPS software. A linear background due to inelastic scattering processes was subtracted. For the fitting of the Pt-4f core level region, the following parameters were used: (i) a spin−orbit coupling energy (separation of $4f_{7/2}$ and $4f_{5/2}$ doublet) $\Delta E = 3.33$ eV,[61] (ii) an intensity ratio between the Pt-$4f_{7/2}$ and Pt-$4f_{5/2}$ peaks $I_{4f_{7/2}}/I_{4f_{5/2}} = 0.75$, and (iii) full width at half-maximum height (fwhm) of the different components after annealing of 1.3 ± 0.1 eV for Pt^0, 1.6 ± 0.3 eV for Pt^{2+} in PtO, and 1.9 ± 0.3 eV for Pt^{4+} in PtO_2. In general, broadening of XPS lines can be attributed to the instrumental resolution, core-hole lifetime effects,[62] Franck−Condon effects,[63] and cluster size effects.[64−67] The higher fwhm values obtained for the Pt oxides as compared to metallic Pt are attributed to the contribution of unresolved shake-up, shake-off and related satellite peaks. The present use of different fwhm values for distinct PtO_x species (PtO_2 > PtO) is based on the following arguments: (i) intermediate oxide species that cannot be separated via XPS due to their proximity in BE (e.g., Pt_3O_4 and PtO_2) might be present in our samples, (ii) different stable geometric structures might coexist for a given oxide phase (e.g., α-PtO_2 and β-PtO_2),[5,44] leading to peak broadening, (iii) the presence of disordered and defective surface oxides as well as bulk-like subsurface oxides with the PtO_x species present at the NP surface (e.g., PtO_2) having a more disordered character and wider fwhm, (iv) a different multiplet structure for the main peaks of PtO_x species that will likely be unresolved for the NP samples and will contribute to peak broadening.[68−70] The instrumental resolution of our monochromatic XPS system, measured on a Au(111) single crystal, is fwhm = 0.9 eV. The BE resolution is estimated to ±0.1 eV.

Results

A. Morphological and Structural Characterization (AFM, TEM). Figure 1 displays AFM images of size-selected Pt NPs supported on SiO_2(4 nm)/Si(001) (a−c), ZrO_2(6 nm)/SiO_2/Si(001) (d−f), and TiO_2(7 nm)/Ti(6 nm)/SiO_2/Si(001) (g−i) taken after in situ O_2-plasma exposure at RT (a,d,g), and after subsequent isochronal annealing in UHV (b,e,h) and in O_2 (c,f,i)

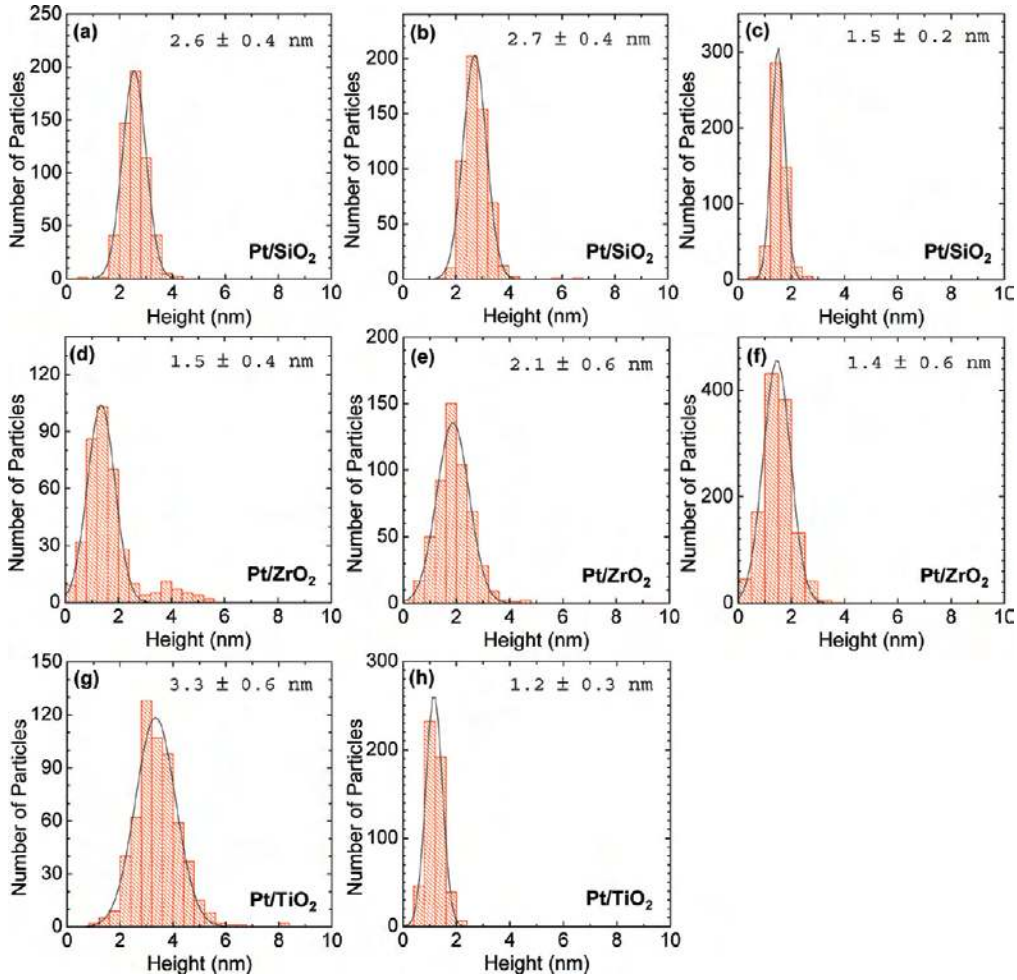

Figure 2. Height histograms of Pt nanoparticles deposited on (a−c) SiO_2, (d−f) ZrO_2, and (g,h) TiO_2 obtained from the analysis of AFM images taken after O_2-plasma treatments for polymer removal (a,d,g), and after subsequent annealing at 1000 K in UHV (b,e,h) and in O_2 (c,f).

($P[O_2] = 1 \times 10^{-4}$ mbar) from 350 to 1000 K in 50 K steps for 10 min. The AFM images in the second and third columns were obtained after the last annealing step at 1000 K. The corresponding NP height histograms are shown in Figure 2 and the average values in Table 1. No significant change in the average NP height is observed for the Pt/SiO_2 and Pt/ZrO_2 systems after annealing in UHV (samples #1b, 2b, respectively, within the error margins of the AFM measurements), but a strong reduction in the NP height is observed for Pt/TiO_2 (sample #3b). The former effect is attributed to the change in the morphology of the ultrathin TiO_2 film upon annealing and the diffusion of the Pt NPs into the TiO_2 substrate, as will be described later based on TEM and XPS data. The initial rougher morphology of the ZrO_2 and TiO_2 substrates as compared to SiO_2/Si(001) is expected to induce errors in the estimation of the NP height on these substrates (Supporting information Figure 2). However, similar NP sizes as in the case of SiO_2 are expected from our micelle encapsulation NP preparation method before annealing.

After annealing in O_2 at 1000 K (samples labeled "c" in Table 1), particle height distributions of 1.5 ± 0.2 nm and 1.4 ± 0.6 nm were obtained for Pt/SiO_2 and Pt/ZrO_2(6 nm), respectively (Figure 2c,f). Those values are smaller than the average values obtained upon NP annealing in UHV (2.7 ± 0.4 nm and 2.1 ± 0.6 nm, respectively). When the same treatment was applied to the Pt/TiO_2 sample, an enhanced substrate roughness was observed, making difficult the distinction between Pt NPs and TiO_x clusters formed on the surface of the TiO_2 film, Figure 1i.

Figure 3 displays cross sectional TEM images of Pt NPs supported on SiO_2 (∼4 nm) (a), ZrO_2 (∼6 nm) (b), and TiO_2 (∼7 nm) (c) after an O_2-plasma treatment at RT (polymer removal) (b,c) and subsequent isochronal annealing in UHV from 350 to 1000 K (a). The SiO_2 film was found to be amorphous. Lattice fringes with d-spacing of $d_{(211)} = 0.232$ nm, $d_{(111)} = 0.298$ nm, and $d_{(11\bar{1})} = 0.313$ nm were observed in Figure 3b, indicating the crystallization of our ultrathin ZrO_2 films into the monoclinic-ZrO_2 phase.[71−73] Some degree of crystallinity was also observed in certain regions of the annealed TiO_2 film supported on metallic titanium. From our TEM data, the structure of the TiO_2 film cannot be conclusively resolved, since the d-spacing obtained [0.327(4) nm] is compatible with rutile, anatase, and brookite TiO_2,[74] and mixed phase domains might also be present in these samples. The shape of the Pt NPs can also be inferred from the images in Figure 3, although higher resolution images are shown in Figure 4 for this purpose. Nearly spherical Pt NPs are observed on SiO_2 after annealing at 1000 K and on ZrO_2 and TiO_2 after an O_2-plasma treatment at RT.

Figure 4 shows high-magnification TEM images of isolated Pt NPs supported on SiO_2 (∼4 nm) (a), ZrO_2 (∼6 nm) (b), and TiO_2 (∼7 nm) (c) after an O_2-plasma treatment (a−c) and subsequent isochronal annealing in UHV from 350 to 1000 K (d−f). Single crystalline Pt NPs are observed in some of the images even before annealing (Figure 4a−c). The lattice spacings measured after atomic oxygen exposure at RT [d = 0.215(4), 0.232(4), 0.282(4) nm, Figure 4a,b,c], are in agreement with those previously reported for PtO_x species,[5,75,76] namely, $d_{(110)} = 0.2137$ nm in PtO, $d_{(211)} = 0.228$ nm in Pt_3O_4, $d_{(200)} = 0.279$ nm in Pt_3O_4, or $d_{(100)} = 0.266$ nm in PtO_2.[77,78] However, the lower values also fit metallic Pt. The identification of surface

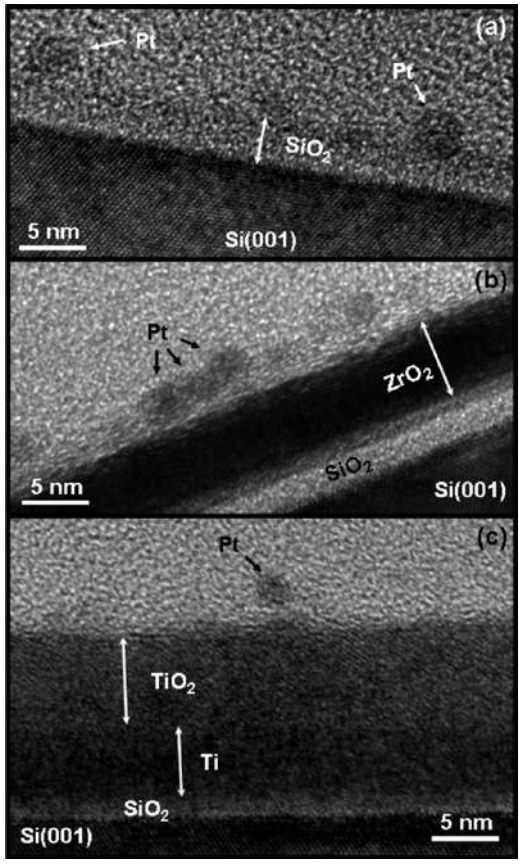

Figure 3. Cross sectional TEM images of Pt nanoparticles supported on (a) SiO_2 (4 nm)/Si(001), (b) ZrO_2 (6 nm)/SiO_2/Si(001), and (c) TiO_2 (7 nm)/Ti (6 nm) acquired after O_2-plasma exposure at RT (b,c) and subsequent in situ isochronal annealing from 350 to 1000 K (a).

oxide phases on small NPs via TEM is very challenging due to several factors, including the possibility of having such phases present in a disordered structural form (amorphous), as well as possible artifacts intrinsic to the TEM technique that could result in local heating of the NPs and the decomposition of unstable surface oxides. Since in our samples PtO_2 species are observed to disappear after annealing in vacuum above 500−600 K (see XPS section), and its content is clearly reduced (giving rise to PtO) well below that temperature, such effect might be responsible for the absence of PtO_2 in the TEM images. Additionally, many of the observed lattice plane spacings can be assigned to different Pt phases, and only a few lattice plane spacings are unique to a specific phase. After annealing in UHV at 1000 K (Figure 4d,e) lattice fringes with spacings of 0.226 and 0.190 nm were measured on the Pt NPs and assigned to the (111) and (200) planes of metallic fcc Pt, respectively.[79] The annealed NPs in our samples are single grain. No clear high-resolution TEM images of the Pt NPs on the thin TiO_2 support could be acquired after annealing. To get insight into the morphology of the Pt/TiO_2 system after annealing, high-angle annular dark-field scanning TEM (HAADF-STEM) images were recorded (Figure 5) and will be discussed below.

From the TEM images in Figure 4, the average shape of our NPs and its thermal evolution was inferred by measuring their aspect ratio (height/diameter). An average of 30 NPs were analyzed in each cross sectional TEM sample, and the corresponding *h*/*d* histograms included in Supporting Information Figures 3−5 and Table 1. Additional high-resolution cross sectional TEM images resolving the shape of Pt NPs on ZrO_2 and TiO_2 supports are also given in Supporting Information Figures 6 and 7. The final results from this analysis together with schematics of model NP shapes are included as insets in Figure 4. After O_2-plasma exposure at RT, the NPs were found to have spherical shape (as expected according to the type of micelles synthesized with PS-P2VP) on all substrates (Figure 4a−c, $h/d \approx 1.0$), indicating weak interaction between the oxidized Pt NPs and the corresponding oxide supports. Sample annealing in UHV at 1000 K did not affect the overall spherical shape of the Pt NPs supported on SiO_2 (Figures 3a and 4d) suggesting weak particle-support interactions in that system.[80] Interestingly, a higher contact area with the support ($h/d \approx 0.7$) was observed for the Pt NPs deposited on ZrO_2 after an analogous annealing treatment in UHV (Figure 4e and Supporting Information Figure 6e−h). The Pt NPs on TiO_2 were found to disappear from the high-resolution real-space TEM images upon annealing at 1000 K in UHV Figure 4f. This result will be explained below.

Figure 5 shows edge-on HAADF-STEM images along the [110] direction of the Si substrate (perpendicular to the [001] Si surface normal) of our Pt/TiO_2 samples after an O_2-plasma treatment at RT (a) and subsequent annealing at 1000 K in UHV (b) and in O_2 ($P[O_2] = 1 \times 10^{-4}$ mbar) (c). Since the differences in atomic numbers between Pt ($Z = 78$) and Ti ($Z = 22$) are sufficiently large, clear contrast between the Pt NPs and the TiO_2 support can be observed in the images of Figure 5. Before annealing (Figure 5a) the Pt NPs were found to be on the surface of the TiO_2 films, while a subsequent annealing in either UHV (Figure 5b) or O_2 (Figure 5c) lead to the diffusion and incorporation of the Pt NPs into the TiO_2 films, leading to completely embedded NPs.

B. Electronic and Chemical Characterization (XPS). ***1. Annealing in UHV.*** Figure 6 shows a set of selected XPS spectra from the Pt-4f core level region of micellar Pt NPs supported on ultrathin SiO_2 (4 nm) (a), ZrO_2 (6 nm) (b), and TiO_2 (7 nm)/Ti (6 nm) (c) films as a function of the annealing temperature. All spectra were measured at room temperature (RT) after O_2 plasma exposure (i), and subsequent annealing in UHV at 500 K (ii), 750 K (iii), and 1000 K (iv) (see Supporting Information Figures 8, 9, and 10 for the complete set of XPS spectra acquired). A wide range of BEs have been reported in the literature for different Pt species.[38,52,59,81] Among the reported values (Supporting Information Table 1), we have selected the Pt-4f BE reference (vertical lines in Figure 6) that best describe the raw data that we obtained on the Pt/SiO_2/Si(001) system, namely, Pt-$4f_{7/2}$ of 71.1 eV for Pt^0, 72.3 eV for PtO, and 73.8 eV for PtO_2. Small deviations with respect to the BE values reported in ref 52 for different PtO_x species were observed while fitting the XPS data of the Pt/SiO_2 system. The latter BEs are shown in the graphs as reference lines for the oxidized Pt NPs deposited on ZrO_2 and TiO_2. The XPS spectra acquired on the Pt/ZrO_2 and Pt/TiO_2 samples after O_2-plasma revealed peak positions for both Pt^{2+} and Pt^{4+} species positively shifted with respect to the above references. The possible origin of these shifts will be discussed below.

It should be mentioned here that the experimental distinction of some of the Pt oxide species is challenging. For example, a Pt species with XPS BE of ∼73.6 eV (Pt-$4f_{7/2}$) has been previously assigned to Pt_3O_4.[82,83] The same authors attribute a BE of 72.2 eV to PtO and 74.2 eV to PtO_2. The assignments are even more complicated when clusters are considered, since positive BE shifts with respect to bulk references may be observed due to electronic initial and final-state effects.[8,57,84] Because of the proximity in BE (∼0.5 eV, see Supporting Information Table 1 for details), Pt_3O_4 and PtO_2 species are

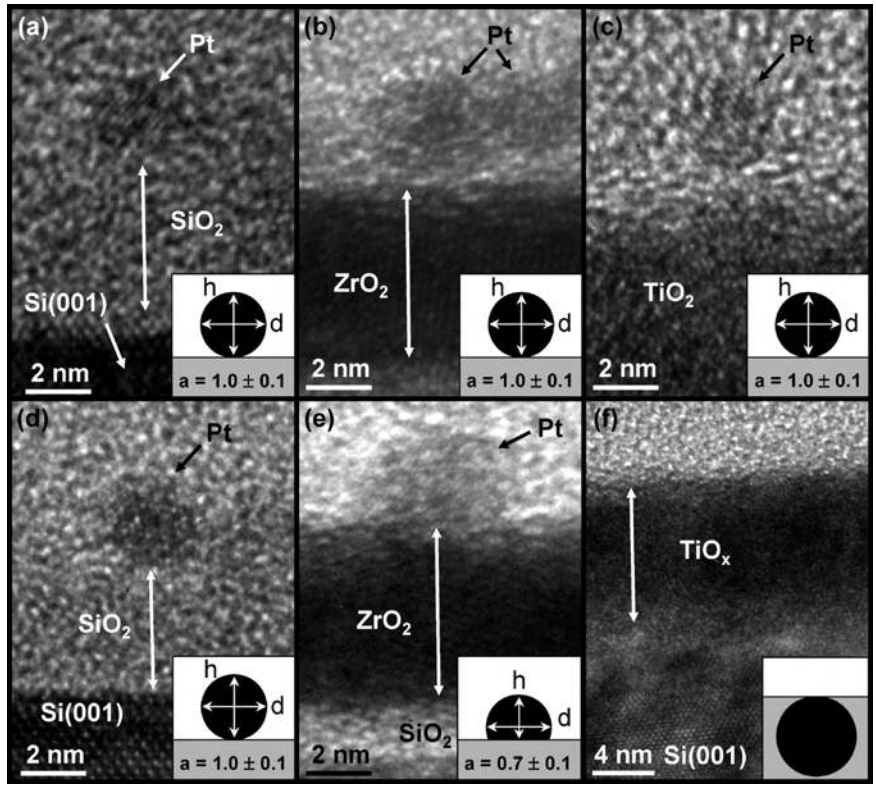

Figure 4. High-magnification cross sectional TEM images of Pt nanoparticles supported on (a,d) SiO_2 (4 nm)/Si(001), (b,e) ZrO_2 (6 nm)/SiO_2/Si(001), and (c,f) TiO_2 (7 nm)/Ti (6 nm) taken after O_2-plasma exposure at RT (a−c) and subsequent in situ isochronal annealing from 350 to 1000 K (d−f). The inset shows representative shapes of Pt nanoparticles on the different supports after the different treatments. The aspect ratios ($a = h/d$) are also indicated.

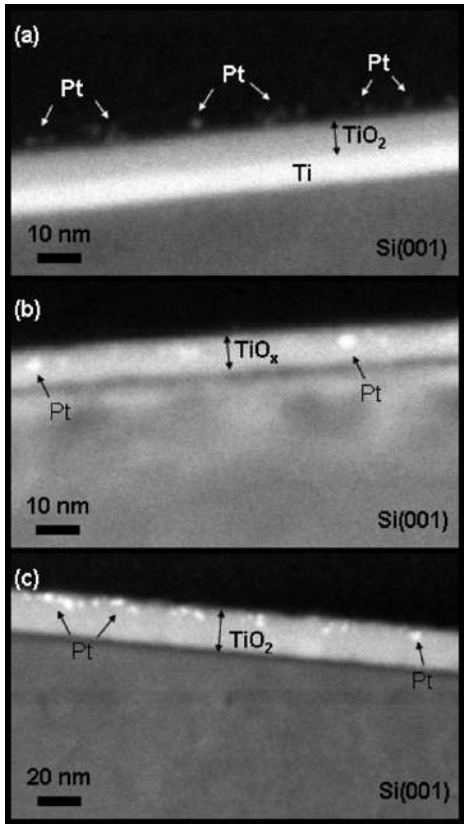

Figure 5. Edge-on STEM images of Pt nanoparticles supported on TiO_2 (7 nm) after (a) O_2-plasma exposure at RT and after subsequent in situ isochronal annealing from 350 to 1000 K in UHV (b) and in O_2 (1×10^{-4} mbar) (c).

not clearly distinguishable via XPS. Alternative techniques such as EXAFS also cannot be used to gain insight into the content of different PtO_x species, since the Pt−O distance for the most common PtO_x species is nearly the same ~2 Å (2.04 Å for PtO, 1.97 Å for Pt_3O_4, 1.99 Å for β-PtO_2).[5,44] In this study, we will refer to the highest BE species detected in our NP samples as PtO_2, since such species is the most commonly reported in the literature, especially on NPs.[41,43,51,85]

Figure 7 shows the effect of annealing on the chemical composition and oxidation state of the NP supports monitored by XPS. Spectra of Pt-free supports (solid lines) and Pt-decorated supports (open circles) are shown simultaneously for comparison purposes. The vertical lines indicate the reference values of the most common oxidation states of the stoichiometric and partially reduced SiO_2,[86,87] ZrO_2,[88,89] and TiO_2[56,90,91] supports, as well as the possible alloys that can be formed with Pt (e.g., Pt−Ti[92] or Pt−Ti−O[20,21]).

Figure 6a demonstrates that the ~3 nm Pt NPs on SiO_2 (sample #1) are completely oxidized upon exposure to atomic oxygen, spectrum (i), with PtO (Pt^{2+}-$4f_{7/2}$ at 72.3 ± 0.1 eV, 33%) and PtO_2 (Pt^{4+}-$4f_{7/2}$ 73.8 ± 0.1 eV, 67%) as main oxide species. Annealing up to 500 K results in a gradual decrease of the PtO_2 signal accompanied by an increase in PtO [Figure 6a (ii)]. Further annealing above 750 K leads to the decomposition of PtO to Pt^0, [Figure 6a (iii,iv)]. In agreement with previous literature,[5,54,55] our XPS data indicate that the direct decomposition of PtO_2 into Pt^0 is not observed; instead, PtO_2 is first reduced to an intermediate oxide species, most likely PtO according to the measured BEs, and then to Pt^0. Complete decomposition of PtO_2 species is observed above 700 K, but a small PtO component could still be fitted to the 1000 K XPS spectrum.

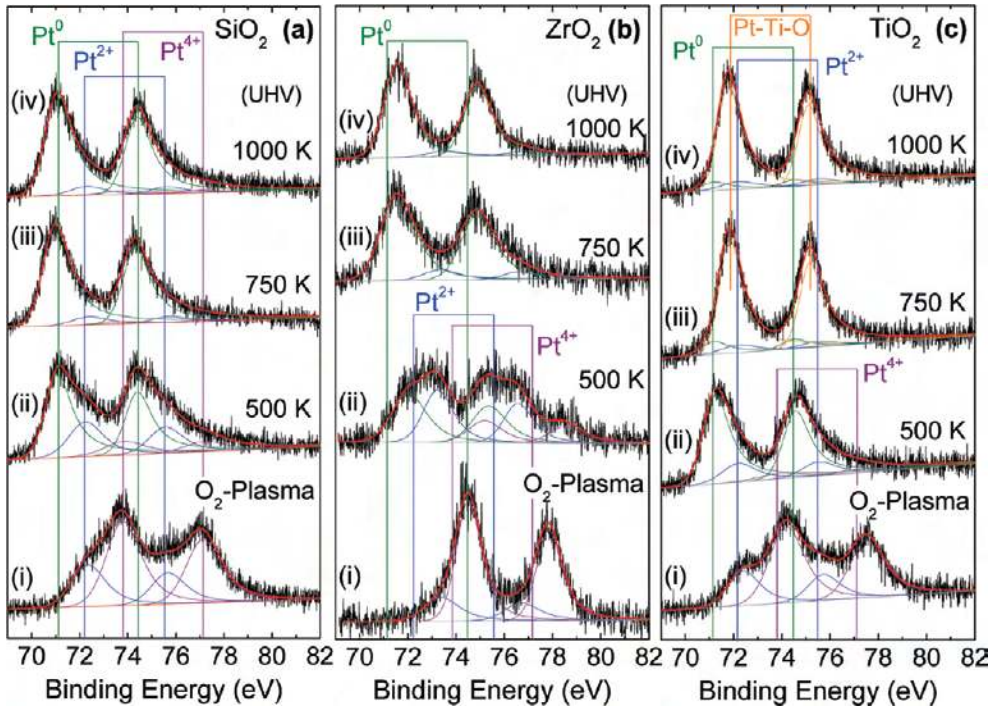

Figure 6. XPS spectra (Al-k_α = 1486.6 eV) corresponding to the Pt-4f core level region of Pt nanoparticles (~3 nm) supported on (a) SiO_2 (4 nm), (b) ZrO_2 (6 nm), and (c) TiO_2 (7 nm)/Ti (6 nm) thin films. The temperature-dependent spectra shown follow the formation of Pt oxide species after (i) O_2-plasma exposure at RT and subsequent in situ isochronal annealing from 350 to 1000 K in 50 K steps for 10 min. Selected annealing temperatures are shown (ii−iv). Solid vertical reference lines signalize the BEs of the spin−orbit doublets characteristic of the different Pt species according to literature values. Least-square fits to the data conducted after background subtraction are also shown. The complete set of XPS measurements are displayed in Supporting Information Figures 8, 9, and 10.

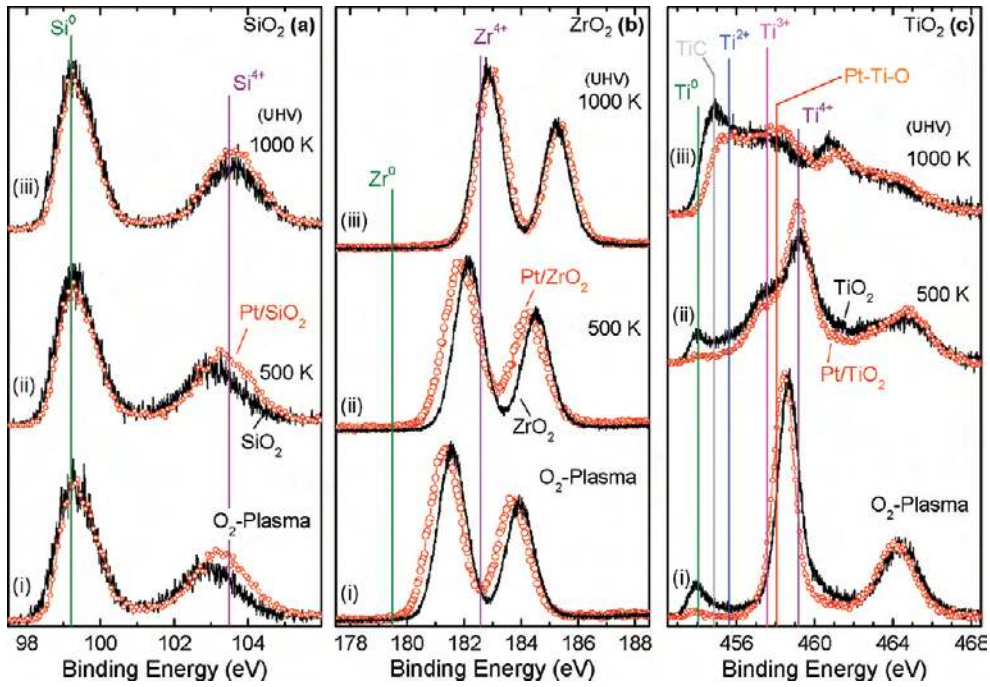

Figure 7. XPS spectra (Al-k_α = 1486.6 eV) corresponding to the Si-2p, Zr-3d, and Ti-2p core levels of (a) SiO_2 (4 nm), (b) ZrO_2 (6 nm), and (c) TiO_2 (7 nm)/Ti (6 nm) thin films with (open circles) and without Pt nanoparticles (solid lines). All samples were subjected to an (i) O_2-plasma exposure at RT and (ii,iii) a subsequent annealing treatment in UHV from 350 to 1000 K in 50 K steps for 10 min. Selected annealing temperatures are shown. Solid vertical reference lines signalize the binding energies of the different oxidation states of the Si-$2p_{3/2}$, Zr-$3d_{5/2}$, and Ti-$2p_{3/2}$ XPS peaks. Least-square fits to the data conducted after background subtraction are also shown in Supporting Information Figures 11, 12, and 13.

No substantial changes in the BE of the Pt^0 and $Pt^{2+,4+}$ species with respect to the reference values is found when comparing the as-prepared samples (after O_2-plasma) and annealed samples.[93] The BE of the SiO_2 component from the Pt/SiO_2 sample is 103.1 eV after atomic oxygen exposure, increasing to 103.5 eV upon annealing at 1000 K [Figure 7a (i) (open circles)]. The increase in the BE of the Pt-coated (open circles) and Pt-free (solid line) SiO_2 thin films with increasing annealing temperature is attributed to band bending.[94] Higher BEs are observed for the Pt-coated supports as compared to pristine SiO_2

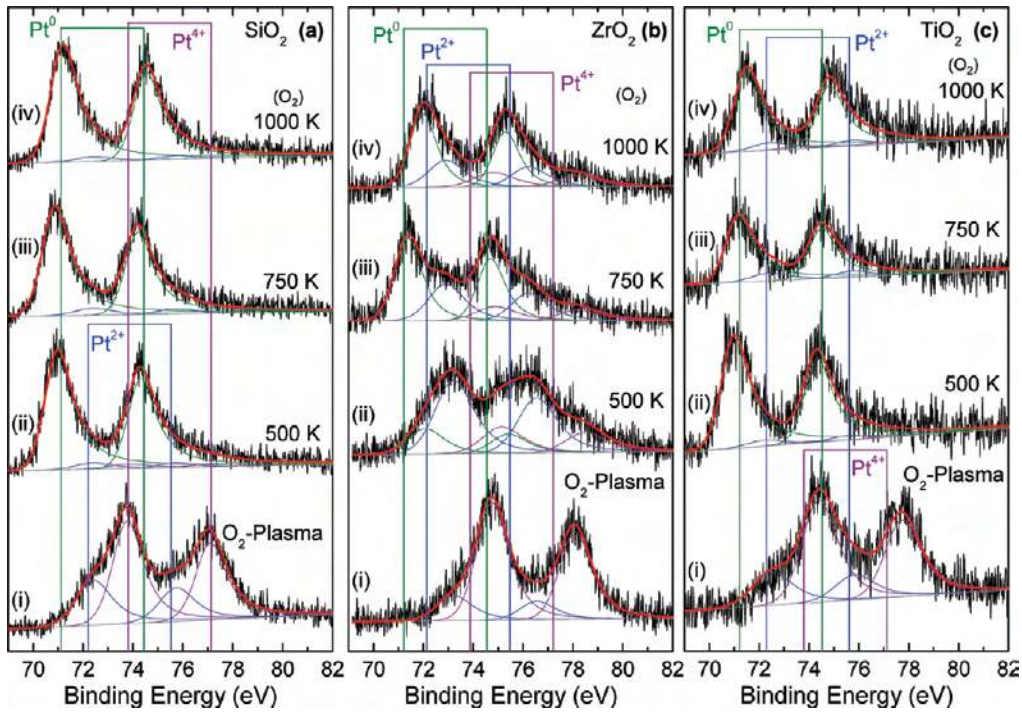

Figure 8. XPS spectra corresponding to the Pt-4f core level region of Pt nanoparticles (~3 nm) supported on (a) SiO_2 (4 nm), (b) ZrO_2 (6 nm), and (c) TiO_2 (7 nm)/Ti (6 nm) thin films. The temperature-dependent spectra shown follow the formation and thermal stability of Pt oxide species after (i) O_2-plasma exposure at RT and (ii−iv) subsequent in situ isochronal annealing treatments from 350 to 1000 K in 50 K steps (for 10 min at each temperature) under an O_2 environment (1×10^{-4} mbar).

below 1000 K.[95] No reduction of the ultrathin SiO_2 films is observed up to 1000 K.

In analogy to the Pt/SiO_2 case, exposure of the Pt/ZrO_2(6 nm) sample to atomic oxygen [Figure 6b (i)] leads to the formation of PtO (21%) and PtO_2 (79%). The BEs of the PtO and PtO_2 species in the Pt/ZrO_2 (6 nm) system are shifted positively with respect to those in Pt/SiO_2 by +1.1 and +0.7 eV, respectively. These high BE values are in good agreement with the BEs measured within our group for similarly prepared Pt NPs supported on nanocrystalline ZrO_2 powder after air or O_2-annealing pretreatments.[9−11] The difference observed between SiO_2 and ZrO_2 might be partially attributed to the slightly larger thickness of the ZrO_2 support employed (6 nm) as compared to SiO_2 (4 nm), which is expected to lead to enhanced charging effects. Nevertheless, the better conductivity of ZrO_2[96] as compared to SiO_2[97,98] should result in smaller BE shifts due to charging, contrary to our present observation. The effect of the oxide support thickness on the measured BE shifts as well as stability of PtO_x species in Pt NP/ZrO_2 will be the object of a subsequent study from our group. Interestingly, in parallel to the positive Pt-4f BE shift, a large negative shift of −1.3 eV with respect to bulk ZrO_2 (Zr^{4+}-$3d_{5/2}$ = 182.6 eV[10,59]) was observed on the Zr-3d region of the Pt/ZrO_2 sample directly after O_2-plasma exposure [Figure 7b (open circles)]. Such negative shift in the Zr-3d peaks is also present on the Pt-free sample (solid lines) to a similar degree (−1.2 eV). On both samples, the bulk-like value of the Zr-3d XPS BE is achieved after sample annealing above 500 K. Above that temperature, the gradual reduction of PtO_2 to PtO and subsequently to Pt^0 is observed. Complete reduction of PtO_2 is observed at 550 K, while a small signal of PtO is still detected at 1000 K.

After atomic oxygen exposure at RT, ~29% PtO and ~71% PtO_2 is obtained for Pt/TiO_2 (sample #3b) [Figure 6c (i)]. Upon annealing (Figure 6c) a gradual decomposition of PtO_2 to PtO (400 K) and subsequently to Pt^0 [spectrum (ii), 500 K] is observed. No PtO_2 species are detected above 550 K while small amounts of PtO persist up to 1000 K. Metallic Pt species are present in this sample above 400 K. Nevertheless, a positive shift of the BE of the Pt component that was previously assigned to metallic Pt is observed above 550 K, signalizing the formation of a Pt−Ti−O alloy[20,21,99] (Pt-$4f_{7/2}$ at 71.9 eV at 750 K versus 71.2 eV at 500 K) [Figure 6c (iii,iv)]. This effect correlates with the onset of TiO_2 reduction at 500 K (Figure 7c) which leads to a stronger Pt/TiO_2 interaction and, according to previous literature as well as to the present TEM data (Figures 4f and 5b), to the encapsulation of Pt by TiO_x[100] or diffusion of Pt into TiO_2. In fact, after O_2-plasma exposure, a majority of Ti^{4+} is detected on the Pt-coated and Pt-free TiO_2 substrates (Figure 7c). However, due to the reduced thickness of our TiO_2 support film (~7 nm based on cross sectional TEM images[56]), lower oxidation states of Ti are also observed, including a small metallic Ti signal from the underlying substrate (more clearly visible on the Pt-free support). A small contribution of Ti^{3+} was observed by XPS in the Pt-coated and Pt-free supports even after O_2 plasma exposure. This component is attributed to the Ti^0−TiO_2 interface. Upon annealing, the thin TiO_2 film (Ti^{4+}) was observed to decompose easily with an increase of the Ti^{3+} from ~5% after O_2-plasma to ~40% after annealing at 500 K [Figure 7c (ii) and Supporting Information Figure 13]. Further increase in the temperature results in a gradual increase of the Ti^{2+} signal, accompanied by a decrease of the content of Ti^{3+} and Ti^{4+} species [Figure 7c (iii)]. In addition, no increase in the Ti^0 component was observed up to 1000 K, but the appearance of TiC (Ti-$2p_{3/2}$ at 454.8 eV) and Pt−Ti−O (Ti-$2p_{3/2}$ at 458.2 eV)[23,101−103] species (Supporting Information Figure 13). The presence of TiC in these samples at 750 K is also corroborated by the sudden appearance of a C-1s XPS signal (not shown) at 281.8 eV.[57] The C present on the surface of sample #3b (Pt-NP/TiO_2 film) after annealing is believed to segregate from the underlying Ti film/SiO_2/Si(001) interface,

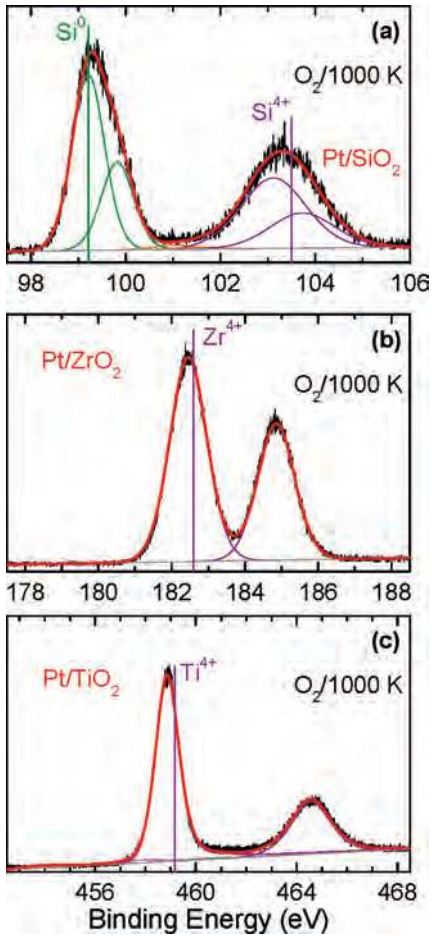

Figure 9. XPS spectra corresponding to the Si-2p, Zr-3d, and Ti-2p core levels of Pt-coated oxide supports: (a) SiO_2 (4 nm), (b) ZrO_2 (6 nm), and (c) TiO_2 (7 nm)/Ti (6 nm). The data were acquired after isochronal annealing in O_2 ($P_{O_2} = 1 \times 10^{-4}$ mbar) from 350 to 1000 K. Solid vertical reference lines signalize the binding energies of the different oxidation states of the Si-$2p_{3/2}$, Zr-$3d_{5/2}$, and Ti-$2p_{3/2}$ XPS peaks.

since such Ti film was deposited ex situ on an untreated Si-wafer before NP dip-coating.[104] Adventitious carbon and carbonyl species (C═O and O═C−O)[105−107] are known contaminants of such native Si substrates. A similar TiO_2 reduction behavior was observed for the Pt-free substrate, also with the appearance of TiC above 600 K [Figure 7c (iii)].

2. Annealing in O_2. After exposing Pt-NP/SiO_2 (sample #1c) to atomic oxygen and subsequent in situ annealing in O_2 (Figure 8a), a similar decomposition pattern of PtO_2 and PtO as compared to the sample annealed in UHV (Figure 6a) is observed.

In contrast, for the Pt-NP/ZrO_2 (6 nm) system (sample #2c), PtO_x species appear to be much more stable during O_2 annealing (Figure 8b) as compared to annealing in UHV (Figure 6b). The XPS spectrum acquired after annealing sample #2c in O_2 at 500 K, Figure 8b (ii) shows ∼19% Pt^0, ∼59% Pt^{2+}, and ∼22% Pt^{4+}. For reference, an analogous thermal treatment in UHV resulted in ∼42% Pt^0, ∼40% Pt^{2+}, and ∼18% Pt^{4+} (Figure 6b). Further annealing in O_2 from 550 to 750 K leads to an increase in the metallic Pt content ∼54% with ∼32% Pt^{2+} and ∼14% Pt^{4+}. Similar ratios of these species are observed after annealing at 1000 K in O_2. The latter trend demonstrates the enhanced stability of the PtO phase on ∼3 nm Pt NPs under O_2,[10] since a lower content of Pt oxide species was detected on the analogous but UHV-annealed sample above 750 K (∼89% Pt^0, ∼11% Pt^{2+}, and ∼0% Pt^{4+}).

The Pt/TiO_2 (sample #3c) system also shows a very different behavior when annealed in O_2 (Figure 8c) as compared to UHV (sample #3b) (Figure 6c). In particular, no Pt−Ti−O alloy formation is observed upon annealing in O_2 at 1000 K [Figure 8c (iv)]. This result is attributed to the lack of O-vacancies in the TiO_2 support when the samples are annealed in O_2.

The effect of the annealing in O_2 on the chemical composition and oxidation state of the NP supports was also monitored by XPS. Figure 9 shows representative XPS spectra of the Si-2p (a), Zr-3d (b), and Ti-2p (c) core levels of Pt/SiO_2, Pt/ZrO_2 and Pt/TiO_2 samples, respectively, acquired after the last step of annealing in O_2 at 1000 K. Our XPS data demonstrate the lack of reduction of any of the supports under our experimental conditions. This is in contrast with our observations for TiO_2 after annealing in UHV [Figure 7c (iii)].

Discussion

A. NP Morphology. The morphology of our samples was inferred based on AFM and TEM measurements. Our data demonstrate the homogeneous size and spatial arrangement of our micellar Pt NPs in several oxide supports. In addition, the evolution of the oxidation state and average shape of our NPs was monitored as a function of different in situ treatments, including atomic oxygen exposure at RT and thermal treatments up to 1000 K in UHV and in O_2. A drastic decrease in the height of Pt NPs is observed after annealing in an O_2 environment (Figure 2c,f). The loss of Pt was confirmed by the decrease in the integrated areas of the Pt-4f XPS peaks. According to refs 108 and 109, the formation and subsequent desorption of volatile PtO_x species might underlie this observation. The former effects were also observed when identical Pt NPs were annealed in UHV, suggesting a thermally induced desorption of Pt atoms or small metallic Pt clusters due to their expected reduced melting temperature (size-effects).[110−112] On the basis of the lattice spacings measured by TEM, a distinction between a possible PtO_x shell and a metallic Pt core (if at all present) cannot be made. In addition, the possible presence of interfacial PtO_x on our NP/oxide support system, suggested by the small PtO component obtained from the fit of our XPS data at 1000 K, could not be clarified based on the cross sectional TEM images.

Regarding the NP shape, the TEM images indicate the initial formation of spherical NPs via our micelle encapsulation method. Nevertheless, the final NP shape was found to be strongly influenced by the post-preparation treatment as well as by the strength of the NP/support interactions. Nearly spherical NPs were observed before annealing on all oxide supports. Interestingly, no change in the NP shape was observed for the Pt/SiO_2 system. This is in contrast with some previous reports[113,114] where strong adhesion and significant wetting of Pt NPs on SiO_2 surfaces was observed upon annealing at 773 K. The reason for this distinct behavior might be related to the inherent nature of our NP preparation method (micelle encapsulation) as well as to the post-deposition O_2-plasma treatment conducted on our samples.[115] When the same NPs are deposited on ZrO_2, a change in the aspect ratio of the NPs (flattening) is observed upon annealing (Figure 4e) highlighting the stronger NP/support interactions present in the case of the Pt-ZrO_2 system that result in an increased contact area of the Pt NPs with the underlying ZrO_2 susbtrate.[10,11] A clear example of strong NP/support interactions is provided by the Pt/TiO_2 system, since the Pt NPs were found to become embedded into the TiO_2 support upon annealing at 1000 K.

Quantitative information on the interaction of the Pt NPs with the different supports, in particular, their adhesion energy (W_{adh}),

was extracted based on contact angle analysis of the cross sectional TEM images (Figures 3, 4 and Supporting Information Figures 6 and 7).[116] The latter analysis is based on the Wulff−Kaischew theorem (eq 1) where the interfacial energy of the metal/support system is obtained from purely geometric characteristics (width-to-height ratio) of the Pt NPs measured by TEM, provided they had the equilibrium shape,[117,118] which is expected after our high temperature annealing treatment. According to Wulff-Kaischew's theorem:

$$\frac{\Delta h}{R} = \frac{W_{adh}}{\gamma_{Pt}} \quad (1)$$

where Δh is the degree of truncation of the NPs at the interface with the support, R is the radius of the truncated sphere, and γ_{Pt} is the surface energy of the principal low-index plane [e.g., Pt(111)]. The formation of Wulff-like Pt NPs using micelle encapsulation methods after high temperature annealing was demonstrated by our group via scanning tunneling microscopy in ref 119.

As shown in Supporting Information Figure 6, the analysis of the contact angle of our NPs was performed by fitting circles to the contour of the Pt NPs in our cross sectional TEM images. The solid lines represent the projections of the interfacial planes. By using the theoretical value[120] of $\gamma_{Pt(111)} = 2.3$ J/m^2, adhesion energies ranging from 0.8 to 2.2 J/m^2 are obtained for the Pt/ZrO_2 system after annealing in UHV at 1000 K. The wide range of W_{adh} might be related to the inhomogeneous nature of our polycrystalline ZrO_2 support film, as well as to the possible stabilization of oxidized Pt−O−Zr or PtO_x species at the NP/support interface. Dewetting is observed for the Pt NP/ZrO_2 system after atomic oxygen exposure, but before annealing (Figure 3b), which is tentatively assigned to the lower surface energy of PtO_x species, γ_{PtO_x}, as compared to metallic Pt.[5,44] Similar results are also observed for the Pt NPs supported on the TiO_2 films after O_2-plasma exposure (Figure 4c and Supporting Information Figure 7).

Regardless of the treatment (O_2 plasma or annealing in UHV at 1000 K), all micellar Pt NPs supported on SiO_2 were found to be spherical in shape, indicating $W_{adh} \approx 0$. This is in clear contrast with our observation for the Pt/ZrO_2 system, where NP flattening was observed after annealing in UHV at 1000 K. Eppler et al.[121] investigated the adhesion of Pt NPs (20 ± 1 nm) fabricated by electron-beam lithography and supported on SiO_2 via AFM. An adhesion energy of ~1 mJ/m^2 was reported for the as-prepared NPs, and annealing at 700 K in 1 atm of H_2 was found to lead to a stronger bonding between the Pt NPs and SiO_2, although no quantitative W_{adh} information was given after annealing. The low adhesion energy obtained by the former group for Pt NPs supported on SiO_2 is in agreement with our findings for the as-prepared spherical micellar NPs. However, in our case no change in the shape of the NPs, and associated increase in adhesion energy, was observed upon annealing. The significantly higher adhesion energies obtained for analogous micellar Pt NPs supported on ZrO_2 after annealing (0.8 to 2.2 J/m^2) highlight the existence of stronger metal/support interactions for this system as compared to SiO_2. Such strong interactions were found to affect the NP morphology upon annealing, leading to a spherical to hemispherical shape transformation. Kasatkin et al.[116] reported similar adhesion energies of ~1.2 J/m^2 for Cu NPs (~4 nm) supported on ZrO_2. In contrast, when Cu islands were supported on SiO_2 or Al_2O_3, much weaker adhesion energies (0.49 and 0.47 J/m^2, respectively) were observed.[122−125] The latter result is in agreement with our findings for micellar Pt/ZrO_2.

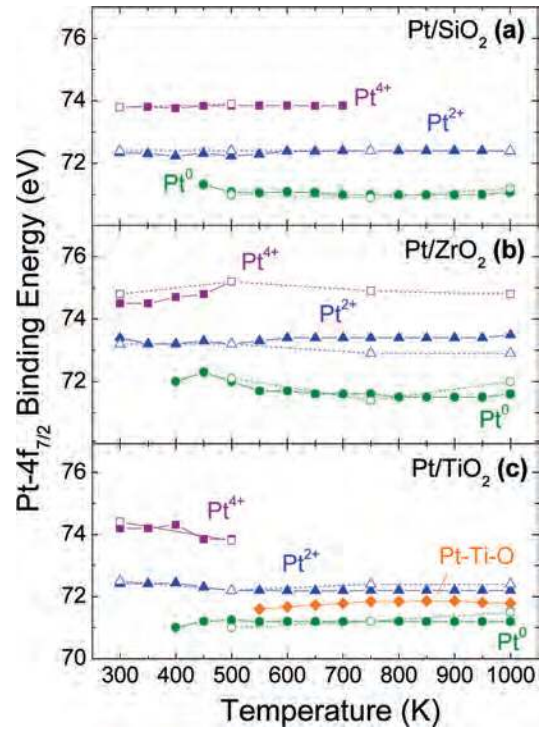

Figure 10. Temperature dependence of the Pt-4$f_{7/2}$ XPS binding energies of Pt nanoparticles (~3 nm) supported on (a) SiO_2 (4 nm), (b) ZrO_2 (6 nm), and (c) TiO_2 (7 nm)/Ti (6 nm) obtained after annealing in UHV (closed symbols, extracted from Figure 6) and in O_2 (open symbols, extracted from Figure 8).

Strong metal/support interactions are expected for the Pt NP/TiO_2 system. On TiO_2(110) and TiO_2 nanocrystalline powders, several groups[20,100,126,127] have shown the encapsulation of Pt NPs by a thin layer of TiO_x upon annealing. Our TEM images indicate that our Pt NPs become completely embedded inside the ultrathin TiO_x films upon annealing at 1000 K in UHV and oxygen (Figure 5b,c), respectively. Interestingly, according to our XPS data (Figures 6 and 8), the formation of Pt−Ti−O alloys is only observed upon annealing in UHV, but not under O_2. This result indicates that even though in both cases the Pt NPs are found to diffuse into the TiO_2 support via TEM, the chemical interaction of the Pt NPs with the support is much stronger when the annealing is conducted in a reducing atmosphere, where vacancies in the TiO_2 support can be readily created. As was mentioned in a previous section, no evidence of TiO_2 reduction was observed by XPS for the Pt/TiO_2 sample annealed in O_2 at 1000 K.

B. Thermal Stability of Pt Oxides. The effect that the nature of the oxide support (e.g., reducibility) has on the thermal stability of Pt oxide species formed on size-selected supported Pt NPs will be discussed here. According to our XPS data, the following trend describes the thermal stability of the different ultrathin film supports (Pt-free) used in our studies from highest to lowest: $SiO_2 > ZrO_2 > TiO_2$/Ti. Although the SiO_2 and ZrO_2 thin film supports have shown similar stability against thermal reduction, both oxides present major differences with respect to their degree of ionic/covalent character,[128] Zr has a much more ionic character, which results in enhanced catalytic reactivity.[7]

Figure 10 shows the changes in the Pt-4$f_{7/2}$ binding energy of the different Pt species detected in the Pt/SiO_2 (4 nm), Pt/ZrO_2 (6 nm), and Pt/TiO_2 (7 nm) samples as a function of the

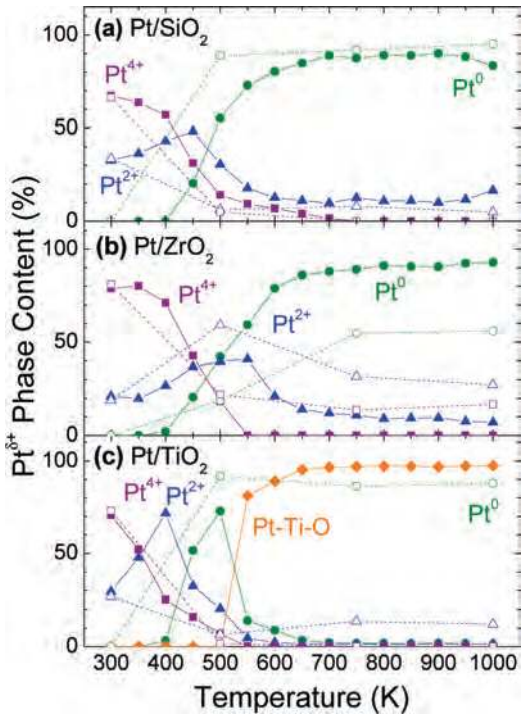

Figure 11. Temperature dependence of the relative content (spectral area) of the different Pt species formed on Pt nanoparticles supported on (a) SiO_2 (4 nm), (b) ZrO_2 (6 nm), and (c) TiO_2 (7 nm)/Ti (6 nm) after annealing in UHV (closed symbols, extracted from Figure 6) and in O_2 (open symbols, extracted from Figure 8).

TABLE 2: Summary of the Content of the Different Pt Species (Pt^0, PtO, PtO_2 and Pt−Ti−O) Obtained from the Least-Square Fit of the XPS Data Acquired on Micellar Pt NPs Supported on SiO_2, ZrO_2, and TiO_2 Thin Films after Annealing in (a) UHV and (b) O_2 ($P = 1 \times 10^{-4}$ mbar) at the Indicated Temperatures for 10 min

	Pt/SiO_2			Pt/ZrO_2			Pt/TiO_2			
(a)	Pt^0	Pt^{2+}	Pt^{4+}	Pt^0	Pt^{2+}	Pt^{4+}	Pt^0	Pt^{2+}	Pt^{4+}	Pt−Ti−O
O_2-plasma	0	33	67	0	21	79	0	29	71	0
500 K	55	31	14	42	40	18	73	20	7	0
750 K	87	13	0	89	11	0	2	1	0	97
1000 K	83	17	0	93	7	0	1	1	0	98
	Pt/SiO_2			Pt/ZrO_2			Pt/TiO_2			
(b)	Pt^0	Pt^{2+}	Pt^{4+}	Pt^0	Pt^{2+}	Pt^{4+}	Pt^0	Pt^{2+}	Pt^{4+}	Pt−Ti−O
O_2-plasma	0	34	66	0	19	81	0	27	73	0
500 K	89	6	5	19	59	22	92	6	2	0
750 K	92	8	0	54	32	14	86	14	0	0
1000 K	95	5	0	56	27	17	88	12	0	0

annealing temperature in UHV (solid symbols) and in O_2 (open symbols). The circles represent Pt^0, the triangles Pt^{2+}, the squares Pt^{4+}, and the rhombus the Pt−Ti−O alloy.

Figure 11 displays the relative content (spectral areas) of the different Pt oxide and Pt−Ti−O species present in our NPs after O_2-plasma exposure and subsequent annealing in UHV (closed symbols) and in O_2 (open symbols). The same labels shown in Figure 10 are used. Table 2 displays the content of the different Pt species obtained from the least-squares fit of XPS data acquired on Pt NPs supported on SiO_2, ZrO_2, and TiO_2 after an O_2-plasma treatment and subsequent annealing in (a) UHV and (b) O_2. A selected set of annealing temperatures is shown.

C. Pt/SiO_2. The BEs of the Pt species in our Pt/SiO_2 NPs (Figure 10a) are higher than those measured on a Pt(111) single crystal after exposure to the same O_2-plasma treatment (not shown). This result is attributed to particle size effects[8] and is in agreement with data from Zhou et al.[129] on 2.5 MLs of Pt deposited on a 5 nm SiO_2 film, where a 70.9 eV BE was measured for Pt-$4f_{7/2}$ right after Pt evaporation, and an additional +0.2 eV shift after annealing at 850 K. The BE change detected by Zhou et al.[129] was attributed to atomic Pt desorption and/or the change in the shape of the Pt islands (from large 2D islands to smaller 3D clusters) resulting in a reduction of the Pt/Si ratio measured by XPS. In our case, the nearly constant BE of the Pt species up to 1000 K also indirectly reflects that no significant changes in our NP size/shape occur at this elevated temperature, in agreement with our AFM (Figure 1 and Table 1) and TEM data (Figures 3 and 4).

Since according to Figure 11a the positions of the XPS peaks assigned to Pt^0 and $Pt^{2+,4+}$ species do not change with increasing annealing temperature, only minimum Pt/SiO_2 interaction appears to be present in this system.[129] This might be an indirect indication of the 3D nature of the NPs supported on SiO_2, with a small NP/support contact area, Figure 4. As has been previously reported, the high thermal stability of SiO_2 (up to ~1093 K)[87] makes the formation of Pt−Si compounds unfavorable. Negligible amounts of Si^+ and Si^{2+} (<3%) were detected in our SiO_2/Si(001) support, Supporting Information Figure 11. This is in contrast to the cases where Pt is in direct contact with Si, readily forming platinum silicides (PtSi and Pt_2Si). Si segregation into Pt(111) has also been observed at annealing temperatures between 750 and 1100 K.[130] Since the BEs of Pt_2Si and PtSi (Pt-$4f_{7/2}$ at ~72.5−73 eV) are very similar to that of PtO in our NPs (~72.3 eV) we cannot completely exclude the formation of Pt-silicides at elevated annealing temperatures.

Figure 11a reveals the initial thermal decomposition of PtO_2 to PtO, with a maximum PtO content observed at 450 K upon annealing in UHV. The latter temperature also corresponds to the onset of Pt^0 formation. These data lead to the conclusion that the decomposition of Pt oxides is a two-step sequential process, with two different activation barriers: $PtO_2 \rightarrow PtO \rightarrow Pt^0$. Similar conclusions were drawn by Seriani et al.[5] based on DFT calculations, although in their case Pt_3O_4 was identified as intermediate Pt oxide species.[54,55] As was mentioned before, our XPS data do not allow us to clearly distinguish Pt_3O_4 from PtO_2 due to their proximity in binding energy, but we can conclude that PtO_2 (or Pt_3O_4, e.g. highest BE Pt species) is not the most stable oxide species on these small NPs.[131] Several other systems display similar reduction mechanisms as the PtO_x, as for example $CuO \rightarrow Cu_2O \rightarrow Cu$.[132]

With increasing annealing temperature in UHV (above 500 K), the Pt^{2+} and Pt^{4+} signals decrease gradually while the Pt^0 component increases, reaching a maximum at ~700 K (Figure 11a). The complete reduction of PtO_2 is observed above 750 K, while a small signal of Pt^{2+} (~13%) remains. The stronger stability of the PtO species on Pt/SiO_2 as compared to Pt/TiO_2 (Figure 11c) might indicate the existence of not just surface but also subsurface and/or interfacial Pt oxides.[93,133] The presence of subsurface oxygen on platinum was previously described by several other groups.[133−137] The possible enhanced stability of PtO_x species at the Pt/SiO_2 interface still needs to be explored. However, such effect is unlikely to be dominant for the latter system due to the small contact area of our 3D NPs with the SiO_2 support, its low reducibility, and the fact that no drastic changes were observed in the decomposition pattern of the Pt/SiO_2 sample upon annealing in UHV [Figure 11a (closed symbols)] versus O_2 [Figure 11a (open symbols)].

D. Pt/ZrO_2. By comparing the Pt-4f BEs of similarly sized Pt NPs supported on different supports (Figure 10b), a positive

BE shift is observed for Pt/ZrO_2 (6 nm) as compared to Pt/SiO_2 and Pt/TiO_2. This effect correlates with a negative BE shift of the Zr-3d features, indicating significant Pt/ZrO_2 interaction. First principle calculations by Jung et al.[138] on $Pt/ZrO_2(111)$ and $Pt_4/ZrO_2(111)$ systems demonstrated strong Pt−Zr interfacial interactions and charge transfer from Pt to Zr atoms. Nevertheless, the preferential adsorption of Pt atoms on oxygen sites in $ZrO_2(111)$ and $ZrO_2(011)$ has been reported by Alfredsson et al.,[139] and contrary to the previous study, no evidence for charge transfer at the Pt/ZrO_2 interface was found. Instead, a charge polarization effect was evoked. Furthermore, although free Pt clusters (Pt_{13} and Pt_{55}) show a symmetric charge distribution with a negatively charged surface and positively charged core, ZrO_2-supported Pt clusters displayed an asymmetric charge distribution with a more positively charged core shifting toward the interface with ZrO_2. The latter results in polarization at the Pt-ZrO_2 interface[138,140] and negative charge accumulation on ZrO_2. Furthermore, the interface of Pt with cubic-ZrO_2 was reported to show insulating properties by Catlow et al.,[141] favoring thus charge accumulation.

He et al.[142] attributed the high thermal stability of their Pt NPs (∼1.4 nm) supported on ZrO_2 to Pt−O interactions in a ZrO_2 matrix. Our XPS data suggest a facile interaction of our Pt NPs with the underlying ZrO_2 substrate and metal−support interaction through Zr, O, or both sites. The possibility of having a small content of Pt−Zr and/or Pt−Zr−O alloy at the NP-support interface cannot be ruled out for the Pt/ZrO_2 (6 nm) system, since after annealing the TEM image in Figure 4e shows the larger wetting of the ZrO_2 support by Pt as compared to SiO_2, indicating stronger adhesion. The temperature range of 773 to 873 K has been reported as onset temperature for alloy formation in Pt/ZrO_2.[143−145] In our studies, the easier reduction of the ZrO_2 film due to its limited thickness (∼6 nm) could play a role in the earlier onset of Pt−Zr or Pt−Zr−O interfacial alloy formation (550 K).

Similar to the Pt/SiO_2 case, Pt/ZrO_2 (6 nm) (Figure 11b) shows the initial stabilization of PtO and PtO_2 species after O_2-plasma exposure. The onset of PtO_2 decomposition occurs above 350 K in UHV (closed symbols). In parallel, the PtO content is found to increase above that temperature, signalizing the onset of the $PtO_2 \rightarrow PtO$ decomposition process. A further increase in the annealing temperature under a UHV environment leads to the decomposition of PtO to Pt^0 on ZrO_2 (6 nm). In contrast, highly stable Pt^{2+} species are detected on the Pt/ZrO_2 system up to 1000 K upon annealing in O_2 (Figure 11b). Such effect might be related to strong Pt−Zr−O interactions at the NP/support interface. PtO_2 fully decomposes after annealing in UHV at 550 K on Pt/ZrO_2 (6 nm). On the other hand, the stability of Pt^{4+} species up to 1000 K is observed on the Pt/ZrO_2 system upon annealing in O_2 [Figure 11b (open squares)].[41]

XPS investigations by Guo et al.[146] revealed the chemical stability of ZrO_2 films (1−5 ML) deposited on Pd(110) when annealed in oxygen at 1000 K. However, the ZrO_2 films were found to reduce above 840 K in UHV, which lead to the formation of Zr−Pd alloys.[146] In agreement with the previous study, the annealing of our Pt NPs supported on ZrO_2 in an O_2 environment up to 1000 K [Figure 11b (open symbols)] neither lead to ZrO_2 reduction (Figure 8b) nor to the formation of a Pt−Zr alloy (Figure 11b (open symbols)]. It did however result in the enhanced stability of PtO_x species. The BE values obtained in this work for such species are in good agreement with those previously measured by our group on similarly prepared Pt NPs supported on nanocrystalline ZrO_2 powder after annealing in air and oxygen.[9−11] In our studies, the high BEs of the Pt-4f peaks (and low BEs of Zr-3d) observed on Pt/ZrO_2 as compared to Pt/SiO_2 and Pt/TiO_2 are attributed to strong Pt-NP/ZrO_2 interactions (charge transfer and possible interface polarization effects), as well as to the likely changes in the ZrO_2 structure after atomic oxygen exposure as well as with increasing annealing temperature. Gottardi et al.[72] have observed changes in the structure of ZrO_2 films deposited on silicon under a gas mixture of Ar/O_2 plasma by XRD. Under a pure Ar plasma, the cubic and tetragonal phases of ZrO_2 were observed, while the more stable monoclinic phase was obtained[147] after adding ∼20% of O_2 to the gas mixture. Furthermore, their XPS measurements showed lower BEs (−0.5 eV) for Zr^{4+} in the ZrO_2 films synthesized in the presence of O_2 as compared to the films deposited in pure Ar.[72] Mondal and Ram[148] also reported changes in the BEs of Zr^{4+}-$3d_{5/2}$ in ZrO_2 measured by XPS as a function of the crystalline structure of ZrO_2, with slightly lower BEs for *c*- (182.0 eV), *t*- (182.0 eV), and *m*-ZrO_2 (182.2 eV) as compared to amorphous ZrO_2 (182.8 eV). In our work, the lowest BEs for the Zr-3d peaks were measured directly after O_2-plasma exposure. A monotonic increase in the Zr^{4+} BE is observed with increasing annealing temperature, reaching a maximum value of 183.0 eV after annealing at 800 K. Furthermore, the intermixing of the ultrathin ZrO_2 film and SiO_2 present at the $ZrO_2/SiO_2/Si(001)$ cannot be ruled out. Such interaction could result in the formation of zirconium silicate.[149]

E. Pt/TiO_2. Figure 11c shows a similar two-step Pt oxide decomposition pattern for Pt/TiO_2 (7 nm)/Ti (6 nm) (sample #3b) as compared to Pt/SiO_2 (sample #1b) in UHV (closed symbols). However, the maximum in the Pt^{2+} content is observed to occur at a slightly lower temperature (∼400 K). With increasing annealing temperature in UHV, the onset of Pt−Ti−O alloy formation is observed at ∼550 K (Figures 6c and 7c). The formation of a Pt−Ti−O alloy is based on the observation of positive BE shifts for the Pt-$4f_{7/2}$ [Figure 10c (closed symbols)] and Ti-$2p_{3/2}$ components (Figure 7c). The Pt-$4f_{7/2}$ peak of the Pt−Ti−O alloy is observed to shift +0.7 eV with respect to the Pt^0 reference line (71.1 eV). The Ti-$2p_{3/2}$ of the Pt−Ti−O alloy component shifts +4.2 eV from the Ti^0 reference line (454.0 eV). Chen et al.[92] observed XPS BE shifts of +0.4 and +1.3 eV for the Pt-4f and Ti-2p peaks of $Pt_3Ti(111)$ with respect to the same two references, respectively. The much larger change in the Ti-2p BE[150] of our samples is attributed to the presence of O in our Pt−Ti−O alloys. Calculations by the same authors indicated the existence of a minor charge transfer from Ti to Pt and the hybridization of Pt-5d and Ti-3d electronic states. The strength of the Pt−Ti bond was observed to be higher than that of the Pt−Pt and Ti−Ti bonds.[92] In our studies, the assignment of the Pt−Ti−O BE is done by comparing the XPS spectra of the Pt/TiO_2/Ti sample [Figure 7c (open circles)] to those of the Pt-free TiO_2/Ti film [Figure 7c (solid line)] after annealing at the same temperatures.

The Pt/TiO_2 system has received great attention in the past due to the observation of strong metal support interaction (SMSI) effects,[22,100] leading to the presence of an ultrathin TiO_x film covering the Pt surface.[20−23,99,126] In the absence of oxygen, Hsieh et al.[151] have shown that the Ti/Pt(100) system had the topmost surface layer composed by pure Pt atoms after annealing in UHV at 1000 K. Zhang et al.[152,153] studied SMSI effects on a Pt/TiO_2-thin film upon sample annealing under an oxidizing environment. Pt was observed to diffuse and substitute Ti atoms in the TiO_2 lattice upon annealing in air at 673 K, becoming oxidized to Pt^{2+}. Sun et al.[99] compared the encapsulation phenomena on Pt (2−2.5 nm)/TiO_2 systems with stoichiometric

and reduced TiO_2 substrates. On the stoichiometric support, annealing above 773 K resulted in the formation of Pt islands with the underlying TiO_2 support remaining fully oxidized. On the contrary, when Pt (2.5 nm)/TiO_x(110) was annealed above 773 K, migration of reduced Ti oxide to the Pt surface and encapsulation was reported. Our AFM images acquired before and after annealing at 1000 K in UHV (Figure 1g,h) indicate an increase in the roughness (rms changes from 0.3 ± 0.1 to 0.5 ± 0.1 nm) of the TiO_2 surface (thin film sample) in sample #3b with increasing temperature, which could facilitate the diffusion of TiO_x on top of the Pt NPs. Such an effect was much less pronounced when the Pt NPs were deposited on the more stable stoichiometric TiO_2(110) single crystal surface.[47] In addition, while the Pt XPS signal does not decrease upon annealing at 1000 K, a much lower apparent NP height (1.2 ± 0.3 nm) is measured by AFM after annealing, suggesting the encapsulation of Pt by TiO_x. This is corroborated by the STEM images displayed in Figure 5b.

As mentioned before, the Pt/SiO_2 and Pt/TiO_2 samples show similar trends upon annealing in O_2, in which a gradual decomposition of Pt^{2+} and Pt^{4+} and an increase of the content of Pt^0species is observed. In clear contrast to the case of the Pt/TiO_2 sample annealed in UHV [Figure 10c (closed symbols)], where Pt−Ti−O alloy formation was observed at high temperature, the lack of O-vacancies in the TiO_2 support upon annealing in O_2 [Figure 8c and 11c (open symbols)] results in the presence of metallic Pt (and not Pt−Ti and/or Pt−Ti−O) in the same temperature regime. Our previous data indicate that the stability of oxides on metal NPs supported on oxide substrates is strongly dependent on the reducibility of the oxide support and annealing environment. These results emphasize the importance of the NP/support interface in determining the electronic, geometric, and chemical properties of the supported NPs. Nevertheless, our TEM data indicate that the encapsulation of Pt by TiO_x or diffusion of the Pt NPs into the TiO_2 support film, takes place irrespective of the annealing environment (UHV or O_2).

Conclusions

We have described the important role played by the NP support on the morphological thermal stability of size-selected Pt NPs as well as on the chemical stability of the different oxide species formed on such NPs upon in situ exposure to atomic oxygen at RT. The synthesis method employed here (micelle encapsulation) allows the deposition of similarly sized, isolated Pt NPs with narrow size distributions on different supports (SiO_2, ZrO_2, and TiO_2 ultrathin films). Thus, size-effects cannot be held responsible for the different behavior (Pt oxide stability) observed for these NPs when supported on distinct substrates.

The following conclusions were extracted from our ex situ AFM, TEM, and in situ XPS studies: (1) no significant changes in the NP size occur after annealing in UHV at 1000 K for the Pt/SiO_2 system, while an apparent decrease in the particle height is observed for Pt/TiO_2. This is attributed to the encapsulation of Pt by TiO_x. The thermal stability of Pt/ZrO_2 seems to be similar to that of Pt/SiO_2, although the enhanced initial roughness of the ZrO_2 support makes the analysis of the NP size after annealing difficult. Our TEM analysis revealed the presence of nearly spherical Pt NPs on SiO_2, ZrO_2, and TiO_2 after atomic oxygen exposure at RT. Annealing in UHV at 1000 K lead to a shape transformation for the Pt/ZrO_2 system (NP flattening), while no changes in the NP shape were observed for Pt/SiO_2. The diffusion of the Pt NPs into the TiO_2 support matrix is observed upon annealing in UHV as well as in O_2 at 1000 K. (2) The most stable Pt oxide species on all three substrates is found to be PtO, becoming nearly completely reduced between 650 and 700 K, although traces of PtO (possibly stabilized at the NP/support interface) could be observed for all samples up to 1000 K. (3) A two-step thermal decomposition process is observed on all three substrates: $PtO_2 \rightarrow PtO \rightarrow$ Pt-metal. (4) Strong metal−support interactions are detected for Pt/TiO_2 above 550 K with the formation of Pt−Ti−O alloy upon annealing in UHV, while an analogous thermal treatment in O_2 resulted only in the presence of Pt^0 at high temperature. (5) The highest stability of PtO species is found for the Pt/ZrO_2 system upon annealing in O_2.

Our observations of the distinct thermal stability of different Pt oxides on small NPs and the strong effect that the chemical nature of the oxide support has on this stabilization are relevant to a wide variety of applications that Pt NPs have in real-world catalytic processes, where oxidizing environments are likely to be present.

Acknowledgment. The authors are thankful to Dr. Jason R. Croy for stimulating discussions. This work has been made possible thanks to the financial support of the Office of Basic Energy Sciences of the US Department of Energy (DE-FG02-08ER15995).

Supporting Information Available: Additional figures and table. This material is available free of charge via the Internet at http://pubs.acs.org.

References and Notes

(1) King, D. A.; Woodruff, D. P. *The Chemical Physics of Solid Surfaces and Heterogeneous Catalysis*; Elsevier: Amsterdam, 1982; Vol. 4.
(2) Freund, H. J. *Surf. Sci.* **2002**, *500*, 271.
(3) Santra, A. K.; Goodman, D. W. *Electrochim. Acta* **2002**, *47*, 3595.
(4) Arblaster, W. J. *Platinum Metals Rev.* **2005**, *49*, 141.
(5) Seriani, N.; Jin, Z.; Pompe, W.; Colombi Ciacchi, L. *Phys. Rev. B* **2007**, *76*, 155421.
(6) Bernhardt, T. M.; Heiz, U.; Landman, U. *Nanocatalysis*; Springer-Verlag: Berlin, 2007.
(7) Croy, J. R.; Mostafa, S.; Liu, J.; Sohn, Y. H.; Heinrich, H.; Roldan Cuenya, B. *Catal. Lett.* **2007**, *119*, 209.
(8) Croy, J. R.; Mostafa, S.; Liu, J.; Sohn, Y. H.; Roldan Cuenya, B. *Catal. Lett.* **2007**, *118*, 1.
(9) Croy, J. R.; Mostafa, S.; Hickman, L.; Heinrich, H.; Roldan Cuenya, B. *Appl. Catal., A* **2008**, *350*, 207.
(10) Croy, J. R.; Mostafa, S.; Heinrich, H.; Roldan Cuenya, B. *Catal. Lett.* **2009**, *131*, 21.
(11) Mostafa, S.; Croy, J. R.; Heinrich, H.; Roldan Cuenya, B. *Appl. Catal., A* **2009**, *366*, 353.
(12) Norskov, J. K.; Bligaard, T.; Rossmeisl, J.; Christensen, C. H. *Nature Chem.* **2009**, *1*, 37.
(13) Hendriksen, B. L. M.; Frenken, J. W. M. *Phys. Rev. Lett.* **2002**, *89*, 046101.
(14) Kurtz, M.; Strunk, J.; Hinrichsen, O.; Muhler, M.; Fink, K.; Meyer, B.; Woell, C. *Angew. Chem., Int. Ed.* **2005**, *44*, 2790.
(15) Naitabdi, A.; Ono, L. K.; Cuenya, B. R. *Appl. Phys. Lett.* **2006**, *89*.
(16) Valden, M.; Lai, X.; Goodman, D. W. *Science* **1998**, *281*, 1647.
(17) Sinha, A. K.; Seelan, S.; Tsubota, S.; Haruta, M. *Top. Catal.* **2004**, *29*, 95.
(18) Hayashi, T.; Tanaka, K.; Haruta, M. *J. Catal.* **1998**, *178*, 566.
(19) Suchorski, Y.; Wrobel, R.; Becker, S.; Strzelczyk, B.; Drachsel, W.; Weiss, H. *Surf. Sci.* **2007**, *601*, 4843.
(20) Belton, D. N.; Sun, Y. M.; White, J. M. *J. Phys. Chem.* **1984**, *88*, 1690.
(21) Pesty, F.; Steinruck, H. P.; Madey, T. E. *Surf. Sci.* **1995**, *339*, 83.
(22) Dulub, O.; Hebenstreit, W.; Diebold, U. *Phys. Rev. Lett.* **2000**, *84*, 3646.
(23) Matsumoto, T.; Batzill, M.; Hsieh, S.; Koel, B. E. *Surf. Sci.* **2004**, *572*, 127.
(24) Weaver, J. F.; Kan, H. H.; Shumbera, R. B. *J. Phys.: Condens. Matter* **2008**, *20*, 184015.

(25) Devarajan, S. P.; Hinojosa, J. A.; Weaver, J. F. *Surf. Sci.* **2008**, *602*, 3116.
(26) Getman, R. B.; Xu, Y.; Schneider, W. F. *J. Phys. Chem.* **2008**, *112*, 9559.
(27) Saliba, N.; Tsai, Y. L.; Panja, C.; Koel, B. E. *Surf. Sci.* **1999**, *419*, 79.
(28) Campbell, C. T.; Ertl, G.; Kuipers, H.; Segner, J. *Surf. Sci.* **1981**, *107*, 220.
(29) Li, T.; Balbuena, P. B. *J. Phys. Chem. B* **2001**, *105*, 9943.
(30) Hendriksen, B. L. M.; Bobaru, S. C.; Frenken, J. W. M. *Catal. Today* **2005**, *105*, 234.
(31) Alayon, E. M. C.; Singh, J.; Nachtegaal, M.; Harfouche, M.; van Bokhoven, J. A. *J. Catal.* **2009**, *263*, 228.
(32) Singh, J.; Nachtegaal, M.; Alayon, E. M. C.; Stotzel, J.; van Bokhoven, J. A. *Chem. Cat. Chem.* **2010**, *2*, 653.
(33) Dam, V. A. T.; de Bruijn, F. A. *J. Electrochem. Soc.* **2007**, *154*, B494.
(34) Hull, R. V.; Li, L.; Xing, Y. C.; Chusuei, C. C. *Chem. Mater.* **2006**, *18*, 1780.
(35) Gasteiger, H. A.; Kocha, S. S.; Sompalli, B.; Wagner, F. T. *Appl. Catal., B* **2005**, *56*, 9.
(36) Asoro, M. A.; Kovar, D.; Shao-Horn, Y.; Allard, L. F.; Ferreira, P. J. *Nanotechnology* **2010**, *21*.
(37) Goeke, R. S.; Datye, A. K. *Top. Catal.* **2007**, *46*, 3.
(38) Blackstock, J. J.; Stewart, D. R.; Li, Z. *Appl. Phys. A* **2005**, *80*, 1343.
(39) Smith, C. E.; Biberian, J. P.; Somorjai, G. A. *J. Catal.* **1979**, *57*, 426.
(40) Muller, O.; Roy, R. *J. Less-Common Met.* **1968**, *16*, 129.
(41) Despres, J.; Elsener, M.; Koebel, M.; Krocher, O.; Schnyder, B.; Wokaun, A. *Appl. Catal., B* **2004**, *50*, 73.
(42) Abe, Y.; Kawamura, M.; Sasaki, K. *Jpn. J. Appl. Phys.* **1999**, *38*, 2092.
(43) Abe, Y.; Yanagisawa, H.; Sasaki, K. *Jpn. J. Appl. Phys.* **1998**, *37*, 4482.
(44) Seriani, N.; Pompe, W.; Ciacchi, L. C. *J. Phys. Chem. B* **2006**, *110*, 14860.
(45) Nagano, Y. *J. Therm. Anal. Cal.* **2002**, *69*, 831.
(46) Samsonov, G. V. *The Oxide Handbook*, 2nd ed.; Plenum Publishing Corporation: New York, 1982.
(47) Naitabdi, A.; Behafarid, F.; Roldan Cuenya, B. *Appl. Phys. Lett.* **2009**, *94*, 083102.
(48) Kim, K. S.; Winograd, N.; Davis, R. E. *J. Am. Chem. Soc.* **1971**, *93*, 6296.
(49) Bancroft, G. M.; Adams, I.; Coatsworth, L. L.; Bennewitz, C. D.; Brown, J. D.; Westwood, W. D. *Anal. Chem.* **1975**, *47*, 586.
(50) Kirner, U. K.; Schierbaum, K. D.; Gopel, W. *Fresenius' J. Anal. Chem.* **1991**, *341*, 416.
(51) Chen, Y. C.; Sun, Y. M.; Yu, S. Y.; Hsiung, C. P.; Gan, J. Y.; Kou, C. S. *Nucl. Instrum. Methods. Phys. Res. B* **2005**, *237*, 296.
(52) Barr, T. L. *J. Phys. Chem.* **1978**, *82*, 1801.
(53) Held, G.; Jones, L. B.; Seddon, E. A.; King, D. A. *J. Phys. Chem. B* **2005**, *109*, 6159.
(54) Saenger, K. L.; Cabral, C.; Lavoie, C.; Rossnagel, S. M. *J. Appl. Phys.* **1999**, *86*, 6084.
(55) Punnoose, A.; Seehra, M. S.; Wender, I. *Fuel. Process. Technol.* **2001**, *74*, 33.
(56) Ono, L. K.; Roldan Cuenya, B. *J. Phys. Chem. C* **2008**, *112*, 4676.
(57) Ono, L. K.; Sudfeld, D.; Roldan Cuenya, B. *Surf. Sci.* **2006**, *600*, 5041.
(58) Ono, L. K.; Roldan Cuenya, B. *Catal. Lett.* **2007**, *113*, 86.
(59) *NIST X-ray Photoelectron Spectroscopy Database*, version 3.5; http://srdata.nist.gov/xps (Accessed September 10, 2010).
(60) Zhu, J.; Liu, Z. G. *Appl. Phys. A* **2004**, *78*, 741.
(61) Neri, G.; Rizzo, G.; Arico, A. S.; Crisafulli, C.; De Luca, L.; Donato, A.; Musolino, M. G.; Pietropaolo, R. *Appl. Catal., A* **2007**, *325*, 15.
(62) Taguchi, M.; Uozumi, T.; Kotani, A. *J. Phys. Soc. Jpn.* **1997**, *66*, 247.
(63) Corcoran, C. J.; Tavassol, H.; Rigsby, M. A.; Bagus, P. S.; Wieckowski, A. *J. Power Sources* **2010**, *195*, 7856.
(64) Cheung, T. T. P. *Surf. Sci.* **1984**, *140*, 151.
(65) Parmigiani, F.; Kay, E.; Bagus, P. S.; Nelin, C. J. *J. Electron Spectrosc. Relat. Phenom.* **1985**, *36*, 257.
(66) Luo, K.; Kim, D. Y.; Goodman, D. W. *J. Molec. Catal. A* **2001**, *167*, 191.
(67) Luo, K.; St Clair, T. P.; Lai, X.; Goodman, D. W. *J. Phys. Chem. B* **2000**, *104*, 3050.
(68) Bagus, P. S.; Freeman, A. J.; Sasaki, F. *Phys. Rev. Lett.* **1973**, *30*, 850.
(69) Nelson, A. J.; Reynolds, J. G.; Roos, J. W. *J. Vac. Sci. Technol., A* **2000**, *18*, 1072.
(70) Mendialdua, J.; Casanova, R.; Barbaux, Y. *J. Electron Spectrosc. Relat. Phenom.* **1995**, *71*, 249.
(71) Zhang, D. P.; Fan, P.; Cai, X. M.; Liang, G. X.; Shao, J. D.; Wang, C. J.; Zhang, D. W.; Fan, Z. X. *Solid State Commun.* **2008**, *148*, 22.
(72) Gottardi, G.; Laidani, N.; Micheli, V.; Bartah, R.; Anderle, M. *Surf. Coat. Technol.* **2008**, *202*, 2332.
(73) Sharma, R.; Naedele, D.; Schweda, E. *Chem. Mater.* **2001**, *13*, 4014.
(74) JCPDS of TiO_2. Rutile: 21-1276; Anatase: 21-1272; Brookite: 29-1360.
(75) Vazquez, A.; Pedraza, F. *Appl. Surf. Sci.* **1996**, *99*, 213.
(76) Zakharchenko, N. I. *Russ. J. Appl. Chem.* **2001**, *74*, 1686.
(77) *Powder Diffraction File, Joint Committee on Powder Diffraction Standards*; The International Center for Diffraction Data: Newtown Square, PA.
(78) Hu, Y. S.; Guo, Y. G.; Sigle, W.; Hore, S.; Balaya, P.; Maier, J. *Nat. Mater.* **2006**, *5*, 713.
(79) Teranishi, T.; Hosoe, M.; Tanaka, T.; Miyake, M. *J. Phys. Chem. B* **1999**, *103*, 3818.
(80) Bonzel, H. P. *Phys. Rep.* **2003**, *385*, 1.
(81) Sen, F.; Gokagac, G. *J. Phys. Chem. C* **2007**, *111*, 5715.
(82) Kuribayashi, K.; Kitamura, S. *Thin Solid Films* **2001**, *400*, 160.
(83) Shumbera, R. B.; Kan, H. H.; Weaver, J. F. *Surf. Sci.* **2007**, *601*, 235.
(84) Roldan Cuenya, B.; Baeck, S. H.; Jaramillo, T. F.; McFarland, E. W. *J. Am. Chem. Soc.* **2003**, *125*, 12928.
(85) Pitchon, V.; Fritz, A. *J. Catal.* **1999**, *186*, 64.
(86) Himpsel, F. J.; Mcfeely, F. R.; Talebibrahimi, A.; Yarmoff, J. A.; Hollinger, G. *Phys. Rev. B* **1988**, *38*, 6084.
(87) Koshizaki, N.; Umehara, H.; Oyama, T. *Thin Solid Films* **1998**, *325*, 130.
(88) Nishino, Y.; Krauss, A. R.; Lin, Y. P.; Gruen, D. M. *J. Nucl. Mater.* **1996**, *228*, 346.
(89) Morant, C.; Sanz, J. M.; Galan, L.; Soriano, L.; Rueda, F. *Surf. Sci.* **1989**, *218*, 331.
(90) Leprince-Wang, Y. *Surf. Coat. Technol.* **2002**, *150*, 257.
(91) Bennett, R. A.; Mulley, J. S.; Newton, M. A.; Surman, M. *J. Chem. Phys.* **2007**, *127*, 084707.
(92) Chen, W. H.; Severin, L.; Gothelid, M.; Hammar, M.; Cameron, S.; Paul, J. *Phys. Rev. B* **1994**, *50*, 5620.
(93) Baetzold, R. C.; Apai, G.; Shustorovich, E.; Jaeger, R. *Phys. Rev. B* **1982**, *26*, 4022.
(94) Alay, J. L.; Fukuda, M.; Bjorkman, C. H.; Nakagawa, K.; Yokoyama, S.; Sasaki, S.; Hirose, M. *Jpn. J. Appl. Phys.* **1995**, *34*, L653.
(95) Komiyama, M.; Shimaguchi, T. *Surf. Interface Anal.* **2001**, *32*, 189.
(96) Jeon, T. S.; White, J. M.; Kwong, D. L. *Appl. Phys. Lett.* **2001**, *78*, 368.
(97) Xue, K.; Ho, H. P.; Xu, J. B. *J. Phys. D* **2007**, *40*, 2886.
(98) Markov, S.; Sushko, P. V.; Roy, S.; Fiegna, C.; Sangiorgi, E.; Shluger, A. L.; Asenov, A. *Phys. Status Solidi A* **2008**, *205*, 1290.
(99) Sun, Y. M.; Belton, D. N.; White, J. M. *J. Phys. Chem.* **1986**, *90*, 5178.
(100) Boyes, E. D.; Gai, P. L. *Ultramicroscopy* **1997**, *67*, 219.
(101) Boffa, A. B.; Galloway, H. C.; Jacobs, P. W.; Benitez, J. J.; Batteas, J. D.; Salmeron, M.; Bell, A. T.; Somorjai, G. A. *Surf. Sci.* **1995**, *326*, 80.
(102) Dwyer, D. J.; Cameron, S. D.; Gland, J. *Surf. Sci.* **1985**, *159*, 430.
(103) Greenlief, C. M.; White, J. M.; Ko, C. S.; Gorte, R. J. *J. Phys. Chem.* **1985**, *89*, 5025.
(104) Mizuno, Y.; King, F. K.; Yamauchi, Y.; Homma, T.; Tanaka, A.; Takakuwa, Y.; Momose, T. *J. Vac. Sci. Technol., A* **2002**, *20*, 1716.
(105) Kawase, K.; Tanimura, J.; Kurokawa, H.; Wakao, K.; Inone, M.; Umeda, H.; Teramoto, A. *J. Electrochem. Soc.* **2005**, *152*, G163.
(106) Joubert, O.; Pelletier, J.; Fiori, C.; Tan, T. A. N. *J. Appl. Phys.* **1990**, *67*, 4291.
(107) Salaneck, W. R.; Paton, A.; Clark, D. T. *J. Appl. Phys.* **1976**, *47*, 144.
(108) Simonsen, S. B.; Chorkendorff, I.; Dahl, S.; Skoglundh, M.; Sehested, J.; Helveg, S. *J. Am. Chem. Soc.* **2010**, *132*, 7968.
(109) Ramachandran, A. S.; Anderson, S. L.; Datye, A. K. *Ultramicroscopy* **1993**, *51*, 282.
(110) Morrow, B. H.; Striolo, A. *Nanotechnology* **2008**, *19*, 195711.
(111) Wen, Y. H.; Fang, H.; Zhu, Z. Z.; Sun, S. G. *Phys. Lett. A* **2009**, *373*, 1800.
(112) Wen, Y. H.; Fang, H.; Zhu, Z. Z.; Sun, S. G. *Phys. Lett. A* **2009**, *373*, 272.
(113) Rioux, R. M.; Song, H.; Grass, M.; Habas, S.; Niesz, K.; Hoefelmeyer, J. D.; Yang, P.; Somorjai, G. A. *Top. Catal.* **2006**, *39*, 167.
(114) Yu, R.; Song, H.; Zhang, X. F.; Yang, P. D. *J. Phys. Chem. B* **2005**, *109*, 6940.
(115) Moruzzi, J. L.; Kiermasz, A.; Eccleston, W. *Plasma Phys.* **1982**, *24*, 605.

(116) Kasatkin, I.; Kniep, B.; Ressler, T. *Phys. Chem. Chem. Phys.* **2007**, *9*, 878.
(117) Henry, C. R. *Prog. Surf. Sci.* **2005**, *80*, 92.
(118) Qin, Z. H.; Lewandowski, M.; Sun, Y. N.; Shaikhutdinov, S.; Freund, H. J. *J. Phys. Chem. C* **2008**, *112*, 10209.
(119) Roldan Cuenya, B.; Croy, J. R.; Mostafa, S.; Behafarid, F.; Li, L.; Zhang, Z. F.; Yang, J. C.; Wang, Q.; Frenkel, A. I. *J. Am. Chem. Soc.* **2010**, *132*, 8747.
(120) Vitos, L.; Ruban, A. V.; Skriver, H. L.; Kollar, J. *Surf. Sci.* **1998**, *411*, 186.
(121) Eppler, A. S.; Rupprechter, G.; Anderson, E. A.; Somorjai, G. A. *J. Phys. Chem. B* **2000**, *104*, 7286.
(122) Zhou, J.; Kang, Y. C.; Chen, D. A. *Surf. Sci.* **2003**, *537*, L429.
(123) Campbell, C. T. *Surf. Sci. Rep.* **1997**, *27*, 1.
(124) Peden, C. H. F.; Kidd, K. B.; Shinn, N. D. *J. Vac. Sci. Technol., A* **1991**, *9*, 1518.
(125) Kriese, M. D.; Gerberich, W. W.; Moody, N. R. *J. Mater. Res.* **1999**, *14*, 3019.
(126) Jennison, D. R.; Dulub, O.; Hebenstreit, W.; Diebold, U. *Surf. Sci.* **2001**, *492*, L677.
(127) Tsujimoto, M.; Moriguchi, S.; Isoda, S.; Kobayashi, T.; Komatsu, T. *J. Electron Microsc.* **1999**, *48*, 361.
(128) Guittet, M. J.; Crocombette, J. P.; Gautier-Soyer, M. *Phys. Rev. B* **2001**, *63*, 125117.
(129) Zhou, Y.; Nakashima, M.; White, J. M. *J. Phys. Chem.* **1988**, *92*, 812.
(130) Diebold, U.; Zhang, L. P.; Anderson, J. F.; Mrozek, P. *J. Vac. Sci. Technol., A* **1996**, *14*, 1679.
(131) Hawkins, J. M.; Weaver, J. F.; Asthagiri, A. *Phys. Rev. B* **2009**, *79*, 125434.
(132) Lee, S. Y.; Mettlach, N.; Nguyen, N.; Sun, Y. M.; White, J. M. *Appl. Surf. Sci.* **2003**, *206*, 102.
(133) Gu, Z. H.; Balbuena, P. B. *J. Phys. Chem. C* **2007**, *111*, 9877.
(134) Niehus, H.; Comsa, G. *Surf. Sci.* **1980**, *93*, L147.
(135) Legare, P. *Surf. Sci.* **2005**, *580*, 137.
(136) McMillan, N.; Lele, T.; Snively, C.; Lauterbach, J. *Catal. Today* **2005**, *105*, 244.
(137) Walker, A. V.; Klotzer, B.; King, D. A. *J. Chem. Phys.* **2000**, *112*, 8631.
(138) Jung, C. H.; Ishimoto, R.; Tsuboi, H.; Koyama, M.; Endou, A.; Kubo, M.; Del Carpio, C. A.; Miyamoto, A. *Appl. Catal., A* **2006**, *305*, 102.
(139) Alfredsson, M.; Catlow, C. R. A. *Phys. Chem. Chem. Phys.* **2001**, *3*, 4129.
(140) Jung, C. H.; Ito, Y.; Endou, A.; Kubo, M.; Imamura, A.; Selvam, P.; Miyamoto, A. *Catal. Today* **2003**, *87*, 43.
(141) Catlow, C. R. A.; French, S. A.; Sokol, A. A.; Alfredsson, M.; Bromley, S. T. *Faraday Discuss.* **2003**, *124*, 185.
(142) He, J. H.; Muto, E.; Kunitake, T.; Liu, S. X.; Zhang, S.; Liu, X. M. *Chem. Phys. Lett.* **2008**, *454*, 274.
(143) Szymanski, R.; Charcosset, H. *Platinum Met. Rev.* **1986**, *30*, 23.
(144) Szymanski, R.; Charcosset, H. *J. Mol. Catal.* **1984**, *25*, 337.
(145) Szymanski, R.; Charcosset, H.; Gallezot, P.; Massardier, J.; Tournayan, L. *J. Catal.* **1986**, *97*, 366.
(146) Guo, Q.; Joyner, R. W. *Appl. Surf. Sci.* **1999**, *144*−*145*, 375.
(147) Qunbo, F.; Fuchi, W.; Huiling, Z.; Feng, Z. *Mol. Sim.* **2008**, *34*, 1099.
(148) Mondal, A.; Ram, S. *Chem. Phys. Lett.* **2003**, *382*, 297.
(149) Rayner, G. B.; Kang, D.; Zhang, Y.; Lucovsky, G. *J. Vac. Sci. Technol., B* **2002**, *20*, 1748.
(150) Beard, B. C.; Ross, P. N. *J. Phys. Chem.* **1986**, *90*, 6811.
(151) Hsieh, S.; Matsumoto, T.; Batzill, M.; Koel, B. E. *Phys. Rev. B* **2003**, *68*, 205417.
(152) Zhang, M.; Feng, C.; Jin, Z. S.; Gang, C.; Du, Z. L.; Dang, H. X. *Chin. J. Catal.* **2005**, *26*, 508.
(153) Zhang, M.; Jin, Z. S.; Zhang, Z. J.; Dang, H. X. *Appl. Surf. Sci.* **2005**, *250*, 29.

JP1086703